Eed controls craniofacial osteoblast differentiation and mesenchymal proliferation from the neural crest

Tim Casey-Clyde[1,2,3]*, S. John Liu[1,2,3], Juan Antonio Camara Serrano[4], Camilla Teng[5], Yoon-Gu Jang[5], Harish N. Vasudevan[1,2], Jeffrey O. Bush[5], David R. Raleigh[1,2,3#]

[1]Department of Radiation Oncology, University of California San Francisco, San Francisco, CA, USA
[2]Department of Neurosurgery, University of California San Francisco, San Francisco, CA, USA
[3]Department of Pathology, University of California San Francisco, San Francisco, CA, USA
[4]Helen Diller Family Comprehensive Cancer Center, University of California San Francisco, San Francisco, CA, USA
[5]Department of Cell and Tissue Biology, University of California San Francisco, San Francisco, CA, USA

[#]Author for correspondence: david.raleigh@ucsf.edu

Abstract

The histone methyltransferase Polycomb repressive complex 2 (PRC2) is required for specification of the neural crest, and mis-regulation of neural crest development can cause severe congenital malformations. PRC2 is necessary for neural crest induction, but the embryonic, cellular, and molecular consequences of PRC2 activity after neural crest induction are incompletely understood. Here we show that *Eed*, a core subunit of PRC2, is required for craniofacial osteoblast differentiation and mesenchymal proliferation after induction of the neural crest. Integrating mouse genetics with single-cell RNA sequencing, our results reveal that conditional knockout of *Eed* after neural crest cell induction causes severe craniofacial hypoplasia, impaired craniofacial osteogenesis, and attenuated craniofacial mesenchymal cell proliferation that is first evident in post-migratory neural crest cell populations. We show that *Eed* drives mesenchymal differentiation and proliferation *in vivo* and in primary craniofacial cell cultures by regulating diverse transcription factor programs that are required for specification of post-migratory neural crest cells. These data enhance understanding of epigenetic mechanisms that underlie craniofacial development, and shed light on the embryonic, cellular, and molecular drivers of rare congenital syndromes in humans.

Introduction

The embryonic neural crest is a multipotent progenitor cell population that gives rise to peripheral neurons, glia, Schwann cells, melanocytes, and diverse mesenchymal cells such as osteoblasts, chondrocytes, fibroblasts, cardiac mesenchyme, and cardiomyocytes (Bronner and LeDouarin, 2012; Simões-Costa and Bronner, 2015). Following induction in the neural tube, cranial neural crest cells undergo dorsolateral migration to the pharyngeal arches and differentiate to form craniofacial bones and cartilage (Minoux and Rijli, 2010). To do so, cranial neural crest cells express transcription factors such as *Sox9*, *Sox10*, and *Twist1* that specify cell fate decisions in derivates of the neural crest (Bertol et al., 2022; Cheung et al., 2005). Pre-migratory neural crest cell specification is partially controlled by the epigenetic regulator Polycomb repressive complex 2 (PRC2), an H3K27 histone methyltransferase that is broadly responsible for chromatin compaction and transcriptional silencing (Margueron and Reinberg, 2011). The catalytic activity of PRC2 is comprised of four core subunits: (1) enhancer of zeste homologue 1 (Ezh1) or Ezh2, (2) suppressor of zeste 12 (Suz12), (3) RBBP4 or RBBP7, and (4) embryonic ectoderm development (Eed) (Piunti and Shilatifard, 2021). Eed binds to H3K27 trimethylation peptides (H3K27me3) and stabilizes Ezh2 for allosteric activation of methyltransferase activity and on-chromatin spreading of H3K27 methylation. *Eed* is required for stem cell plasticity, pluripotency, and maintaining cell fate decisions, but all PRC2 core subunits are required for embryonic development and loss of any individual subunit is embryonic lethal around gastrulation (Faust et al., 1995; O'Carroll et al., 2001; Pasini et al., 2004). *Eed* null embryos can initiate endoderm and mesoderm induction but have global anterior-posterior patterning defects in the primitive streak (Faust et al., 1995; Schumacher et al., 1996) and genome-wide defects in H3K27 methylation (Montgomery et al., 2007).

Ezh2 has been studied in the context of pre-migratory neural crest development. In mice, *Wnt1-Cre Ezh2*$^{Fl/Fl}$ embryos fail to develop skull and mandibular structures due to de-repression of Hox transcription factors in cranial neural crest cells (Ferguson et al., 2018; Kim et al., 2018; Schwarz et al., 2014), and loss of *Ezh2* in mesenchymal precursor cells causes skeletal defects and craniosynostosis in *Prrx1-Cre Ezh2*$^{Fl/Fl}$ embryos (Dudakovic et al., 2015). Ezh2 also regulates neural crest specification in xenopus (Tien et al., 2015), and *Col2-Cre Eed*$^{Fl/Fl}$ mice have kyphosis and accelerated hypertrophic differentiation due to de-repression of

Wnt and TGF-β signaling in chondrocytes (Mirzamohammadi et al., 2016). Genetic and molecular interactions allow *Eed* to repress Hox genes to maintain vertebral body identity during mouse development (Kim et al., 2006), but the embryonic, cellular, and molecular consequences of *Eed* activity in craniofacial development are incompletely understood. To address this gap in our understanding of epigenetic mechanisms that may contribute to craniofacial development, we conditionally deleted *Eed* from the migratory neural crest and its derivatives. Our results suggest that *Eed* is required for craniofacial osteoblast differentiation from post-migratory neural crest mesenchymal stem cells, and that *Eed* regulates diverse transcription factor programs that are required for mesenchymal cell proliferation, differentiation, and osteogenesis. More broadly, these data show that *Eed* is required at early post-migratory stages in neural crest progenitors of craniofacial structures.

Results

Loss of Eed after neural crest induction causes severe craniofacial malformations

To determine if *Eed* is required for the development of neural crest derivatives, homozygous floxed *Eed* alleles (*Eed*$^{Fl/Fl}$) (Yu et al., 2009) were used to conditionally delete *Eed* following neural crest cell induction using Cre under control of the *Sox10* promoter, which is expressed in the migratory neural crest at embryonic day E8.75 and results in complete recombination in post-migratory neural crest cells by E10.5 (Matsuoka et al., 2004; Niethamer et al., 2020). *Sox10-Cre Eed*$^{Fl/Fl}$ mice were not recovered past postnatal day 0, suggesting that loss of *Eed* following induction of the neural crest is embryonic lethal (Fig. 1a). *Sox10-Cre Eed*$^{Fl/Fl}$ embryos were recovered at expected genotypic frequencies from embryonic day E9.5 to E17.5 (Fig. 1a), and there were no differences in the penetrance or severity of *Sox10-Cre Eed*$^{Fl/Fl}$ phenotypes whether Cre was maternally or paternally inherited, as has been reported for other phenotypes arising in cells expressing *Sox10-Cre* (Crispino et al., 2011; Luo et al., 2020). No overt phenotypes were identified at early post-migratory neural crest cell stages E10.5 or E11.5, but craniofacial malformations were seen in *Sox10-Cre Eed*$^{Fl/Fl}$ embryos starting at E12.5 that increased in severity throughout the remainder of embryonic development (Fig. 1b). *Sox10-Cre Eed*$^{Fl/Fl}$ phenotypes were broadly consistent with impaired development of craniofacial structures (Ferguson et al., 2018; Schwarz et al., 2014), including frontonasal and mandibular hypoplasia, a prominent telencephalon and exencephaly resulting from underdevelopment of the viscerocranium and frontal calvarium, collapsed nasal cavity bones, and microtia compared to controls (Fig. 1c). *Sox10-Cre Eed*$^{Fl/Fl}$ embryos had increased pupillary distance and craniofacial width (Supplementary Fig. 1a-d), and whole mount DAPI imaging of *Sox10-Cre Eed*$^{Fl/Fl}$ embryos revealed severe frontonasal dysplasia with underdeveloped midface and mandible, and an irregular and corrugated facial structure compared to controls (Fig. 1d). Although PRC2 is ubiquitously expressed in the developing embryo (O'Carroll et al., 2001), *Sox10-Cre Eed*$^{Fl/Fl}$ embryos did not have cardiac outflow tract defects or other structural heart malformations that can arise from impaired neural crest differentiation (Lindsay et al., 2001, 1999; Nakamura et al., 2009) (Supplementary Fig. 2a-d and Movie 1, 2). Instead, fetal echocardiography showed subtle structural and functional changes but preserved ejection fraction and fraction shortening in *Sox10-Cre Eed*$^{Fl/Fl}$ embryos compared to controls (Supplementary Fig. 2d).

Eed regulates craniofacial mesenchymal cell differentiation and proliferation from the early post-migratory neural crest

Skeletal stains, computed tomography (microCT), histology, and immunofluorescence were used to shed light on how loss of *Eed* impacts craniofacial development. Whole mount alcian blue/alizarin red staining of *Sox10-Cre Eed*$^{Fl/Fl}$ embryos revealed hypoplasia of the viscerocranium, including reduced frontal, temporal, maxillary, and mandibular bones, and complete loss of the tympanic ring and premaxillary and nasal bones compared to controls (Fig. 2a, b and Supplementary Fig. 3a). MicroCT validated these findings, showing fragmentation and hypoplasia of the frontal, temporal, maxillary, and mandibular bones, loss of frontal calvarial fusion, and absence of tympanic ring and nasal bones (Fig. 2c-e and Movie 3, 4). H&E histology showed that frontal calvarium reduction resulted in anteriorly displaced brain structures in *Sox10-Cre Eed*$^{Fl/Fl}$ embryos compared to controls, with the midbrain and cortex in the same coronal plane as the nasal cavity and developing mandible (Fig. 3a and Supplementary Fig. 3b). Most of the midfacial and mandible were absent in *Sox10-Cre Eed*$^{Fl/Fl}$ embryos, and the tongue and masseter muscles were underdeveloped (Fig. 3a).

Immunofluorescence demonstrated disorganized ALPL and Osteocalcin, markers of osteoblasts and mineralizing bone (Liu et al., 2018), in craniofacial tissues from *Sox10-Cre Eed*$^{Fl/Fl}$ embryos compared to controls (Fig. 3b and Supplementary Fig. 3c). Immunofluorescence for Sox9, a marker of chondrocytes that are derived from the neural crest (Mori-Akiyama et al., 2003; Yan et al., 2002), was also disorganized in *Sox10-Cre Eed*$^{Fl/Fl}$ embryos compared to controls (Fig. 3b). There was a small increase in immunofluorescence labeling index for cleaved Caspase 3 (Supplementary Fig. 3d, e), suggesting that apoptosis may play a subtle role in

craniofacial phenotypes from *Sox10-Cre Eed*$^{Fl/Fl}$ embryos compared to controls. In contrast to *Wnt1-Cre Ezh2*$^{Fl/Fl}$ embryos (Ferguson et al., 2018; Schwarz et al., 2014), the craniofacial region of *Sox10-Cre Eed*$^{Fl/Fl}$ embryos had marked decreased immunofluorescence labeling index for Ki67 (Fig. 3c, 3d), a marker of cell proliferation (Gerdes et al., 1984), and decreased immunofluorescence staining for Vimentin (Vim), a marker of mesenchymal cells (Mendez et al., 2010) (Fig. 3c). Immunofluorescence for Runx2, a transcription factor that is required for osteoblast differentiation and proliferation (Kawane et al., 2018; Komori, 2009), was also decreased in craniofacial tissues from *Sox10-Cre Eed*$^{Fl/Fl}$ embryos compared to controls (Fig. 3e and Supplementary Fig. 3f). In support of these findings, BrdU labeling index was decreased in the craniofacial region of *Sox10-Cre Eed*$^{Fl/Fl}$ embryos compared to controls (Supplementary Fig. 4a, b), Eed, Runx2, Ki67, and ALPL were decreased in primary *Sox10-Cre Eed*$^{Fl/Fl}$ craniofacial cell cultures compared to controls (Fig. 3f and Supplementary Fig. 4c), and there was no change in immunofluorescence for Sox10 in either primary *Sox10-Cre Eed*$^{Fl/Fl}$ craniofacial cell cultures or *Sox10-Cre Eed*$^{Fl/Fl}$ embryos compared to controls (Supplementary Fig. 4c, e). These results suggest craniofacial mesenchymal differentiation, proliferation, and osteogenesis are impaired in *Sox10-Cre Eed*$^{Fl/Fl}$ embryos (Honoré et al., 2003; Kim et al., 2003).

Eed regulates craniofacial mesenchymal stem cell, osteoblast, and proliferating mesenchymal cell fate from the early post-migratory neural crest

To define cell types and gene expression programs underlying craniofacial phenotypes in *Sox10-Cre Eed*$^{Fl/Fl}$ embryos, single-cell RNA sequencing was performed on litter-matched E12.5 *Sox10-Cre Eed*$^{Fl/WT}$ and *Sox10-Cre Eed*$^{Fl/Fl}$ heads (n=3 biological replicates per genotype). Uniform manifold approximation and projection (UMAP) analysis of 63,730 single-cell transcriptomes revealed 23 cell clusters (C0-C22) that were defined using automated cell type classification (Ianevski et al., 2022), cell signature genes, cell cycle analysis, and differentially expressed cluster marker genes (Fig. 4a, Supplementary Fig. 5, 6, and Supplementary Table 1, 2). Differentiating osteoblasts marked by *Runx2* (C0) and proliferating mesenchymal cells marked by Ki67 (C7) were enriched in *Sox10-Cre Eed*$^{Fl/WT}$ samples (Fig. 4b-d). Mesenchymal stem cells marked by *Col6a3* (C4) or *Dcn* (C5) were enriched in *Sox10-Cre Eed*$^{Fl/Fl}$ samples (Jang et al., 2016; Lamandé et al., 2006) (Fig. 4b-d), suggesting that loss of *Eed* prevents craniofacial mesenchymal stem cell differentiation. There were subtle differences in the number of interneurons (C17, 1.4% versus 1.9% of cells, p=0.01), Schwann cells (C19, 1.0 versus 1.3% of cells, p=0.03), pericytes (C20, 0.7% vs 0.9%, p=0.05), and spinal neurons (C21, 0.5% vs 0.9% of cells, p=0.003) in *Sox10-Cre Eed*$^{Fl/WT}$ versus *Sox10-Cre Eed*$^{Fl/Fl}$ samples, but each of these comprised a small minority of the recovered cell types (Student's t tests) (Supplementary Table 1). There were no differences between genotypes in the number of chondrocytes (C10, 3.1% versus 2.7%, p=0.09), fibroblasts (C11, 2.6% versus 2.7%, p=0.24), endothelia (C16, 1.9% vs 1.6%, p=0.22), hematopoietic cells, or other cell types recovered at E12.5 (Student's t tests) (Supplementary Table 1).

Differential expression analysis of single cell transcriptomes from differentiating osteoblasts (C0), which were enriched in *Sox10-Cre Eed*$^{Fl/WT}$ samples (Fig. 4c), compared to mesenchymal stem cells marked by *Col6a3* (C4), which were enriched in *Sox10-Cre Eed*$^{Fl/Fl}$ samples (Fig. 4c), showed *Sox5* and *Sox6* were reduced in mesenchymal stem cells (Fig. 4e, Supplementary Fig. 7a, and Supplementary Table 3). These data are consistent with the known role of Sox transcription factors in craniofacial specification and development (Smits et al., 2001). Iroquois homeobox (Irx) transcription factors 3 and 5, which contribute to craniofacial osteogenesis and mineralization (Bonnard et al., 2012; Cain et al., 2016; Tan et al., 2020), were also suppressed in mesenchymal stem cells compared to differentiating osteoblasts (Fig. 4e, Supplementary Fig. 7a, and Supplementary Table 3).

Differential expression analysis of single cell transcriptomes from differentiating osteoblasts compared to mesenchymal stem cells marked by *Dcn* (C5), which were also enriched in *Sox10-Cre Eed*$^{Fl/Fl}$ samples (Fig. 4c), showed *Mecom*, *Trps1,* and *Ptch1* were suppressed and *Sparc* and *Tnmd* were enriched in mesenchymal stem cells (Fig. 4f, Supplementary Fig. 7b, and Supplementary Table 4). Loss of *Mecom* causes craniofacial malformations in mice and zebrafish (Shull et al., 2020), *Ptch1* is a key component of the Hedgehog pathway that is crucial for craniofacial osteogenesis (Jeong et al., 2004; Metzis et al., 2013), and *Trps1* regulates secondary palate and vibrissa development (Cho et al., 2019; Fantauzzo and Christiano, 2011). Consistently, *Sox10-Cre Eed*$^{Fl/Fl}$ samples had decreased vibrissa compared to controls (Fig. 1d and Supplementary Fig. 3b). *Sparc* drives morphogenesis of the pharyngeal arches and inner ear (Rotllant et al., 2008), and *Tnmd* regulates mesenchymal differentiation (Shukunami et al., 2006). *Pax3* and *Pax7,* key regulators of neural crest migration and development of skeletal structures (Maczkowiak et al., 2010), were also suppressed in mesenchymal stem cells compared to differentiating osteoblasts (Fig. 4f, Supplementary Fig. 7b, and Supplementary Table 4).

Differential expression analysis of single cell transcriptomes from the two clusters of mesenchymal stem cells that were marked by *Col6a3* (C4) versus *Dcn* (C5), both of which were enriched in *Sox10-Cre Eed*$^{Fl/Fl}$ samples (Fig. 4c), showed *Twist2*, *Irx3*, and *Irx5*, which regulate mesenchymal differentiation to osteoblasts (Lee et al., 2000; Tamamura et al., 2017; Tan et al., 2020), distinguished mesenchymal stem cell populations (Fig. 4g, Supplementary Fig. 7c, and Supplementary Table 5).

To determine if there were differences in the gene expression programs from differentiating osteoblasts (C0), mesenchymal stem cells (C4, C5), or proliferating mesenchymal cells (C7) in *Sox10-Cre Eed*$^{Fl/WT}$ versus *Sox10-Cre Eed*$^{Fl/Fl}$ samples, differential expression analysis was performed on single-cell transcriptomes from these clusters between genotypes (Supplementary Table 6). Consistent with craniofacial findings after loss of *Ezh2* (Ferguson et al., 2018; Kim et al., 2018; Schwarz et al., 2014) and vertebral body findings after loss of *Eed* (Kim et al., 2006), Hox transcription factors were broadly de-repressed in mesenchymal cell populations from *Sox10-Cre Eed*$^{Fl/Fl}$ samples compared to controls (Fig. 4h). PRC2 targets Sp7 in bone marrow stroma cells (Liu et al., 2013) and regulates Wnt signaling in dental stem cells (Jing et al., 2016). Differential expression analysis showed that *Sp7* was enriched in mesenchymal single-cell transcriptomes from *Sox10-Cre Eed*$^{Fl/WT}$ samples and the Wnt and stem cell regulator gene *Gata4* was enriched in mesenchymal single-cell transcriptomes from *Sox10-Cre Eed*$^{Fl/Fl}$ samples (Fig. 4h). *Mki67*, *Pax3*, and *Pax7* were enriched in mesenchymal single-cell transcriptomes from *Sox10-Cre Eed*$^{Fl/WT}$ samples, and the cell cycle inhibitors *Cdkn2a* and *Cdkn2b* were enriched in mesenchymal single-cell transcriptomes from *Sox10-Cre Eed*$^{Fl/Fl}$ samples (Fig. 4h). In sum, these data show that *Eed* specifies craniofacial osteoblast differentiation and mesenchymal cell proliferation by regulating diverse transcription factor programs that are required for specification of post-migratory neural crest cells, and that loss of *Eed* inhibits mesenchymal stem cell differentiation and mesenchymal cell proliferation. These data contrast with the function of *Eed* in chondrocytes, where genetic inactivation of *Eed* at a later stage in mesenchymal development accelerates hypertrophic differentiation, leading to hypoxia and cell death (Mirzamohammadi et al., 2016).

Discussion

Epigenetic regulation of the neural crest, which differentiates into diverse mesenchymal derivatives, is incompletely understood. Here we identify the PRC2 core subunit *Eed* as a potent regulator of craniofacial development after induction of the neural crest. Conditional deletion of *Eed* using *Sox10-Cre* causes severe craniofacial malformations that are consistent with impaired differentiation and proliferation of cells arising from the pharyngeal arches (Frisdal and Trainor, 2014). In support of this hypothesis, we observed severe defects in the development of craniofacial mesenchyme-derived tissues (Fig. 1, 2) that were consistent with molecular and cellular findings from *Sox10-Cre Eed*$^{Fl/Fl}$ embryos (Fig. 3, 4). Expression of key regulators of craniofacial osteogenesis such as *Runx2, Irx3*, *Irx5, Mecom, Trps1, Ptch1, Pax3,* and *Pax7* were reduced in *Sox10-Cre Eed*$^{Fl/Fl}$ heads and primary craniofacial cell cultures compared to controls, and single-cell RNA sequencing showed reduced craniofacial osteoblast differentiation and reduced proliferation of mesenchymal cells in *Sox10-Cre Eed*$^{Fl/Fl}$ heads compared to controls. We also identified subtle cardiac phenotypes and a small increase in apoptosis in *Sox10-Cre Eed*$^{Fl/Fl}$ embryos. These data suggest that PRC2 may contribute to the development of diverse neural crest-derived tissues but is particularly important for craniofacial mesenchymal cell differentiation and proliferation.

By using *Sox10-Cre*, which marks the migratory neural crest (Matsuoka et al., 2004), we bypass potential roles of *Eed* in neural crest cell induction to examine its function in neural crest cell development. The requirement of PRC2 for craniofacial development has been studied in the context of *Ezh2* loss using *Wnt1-Cre* (Ferguson et al., 2018; Schwarz et al., 2014), but to our knowledge, our study is the first report directly linking *Eed* to differentiation of neural crest-derived mesenchymal cells. To date, fifteen human missense mutations in *EED* have been reported as pathogenic for Cohen-Gibson syndrome (Cohen and Gibson, 2016; Cohen et al., 2015; Goel et al., 2024). Like Weaver syndrome, which arises from missense mutations in *EZH2* (Gibson et al., 2012; Tatton-Brown et al., 2013), and Imagawa-Matsumoto syndrome, which arises from missense mutations in *SUZ12* (Imagawa et al., 2018), Cohen-Gibson syndrome is a rare congenital syndrome associated with craniofacial malformations, advanced bone age, intellectual disability, and developmental delay (Spellicy et al., 2019). *EED* mutations in individuals with Cohen-Gibson syndrome cluster in WD40 domains 3 through 5 and are predicted to (1) abolish interaction with EZH2, (2) prevent histone methyltransferase activity, and (3) inhibit H3K27 trimethylation peptide binding. In support of these hypotheses, functional investigations have shown that single nucleotide variants in the WD40 domain of *EED* abolish binding to *EZH2 in vitro* (Denisenko et al., 1998). Mouse models encoding pathogenic *EZH2* missense variants, which are predicted to result in loss of function of the PRC2 complex, phenocopy Weaver syndrome and cause excess osteogenesis

and skeletal overgrowth (Gao et al., 2023). In this study, we show that loss of *Eed* after neural crest induction causes the opposite phenotype, resulting in craniofacial hypoplasia due to impairments in osteogenesis, mesenchymal cell proliferation, and mesenchymal stem cell differentiation. The discrepancy of missense variants in *EED* causing gain of craniofacial osteogenic function in humans versus loss of *Eed* causing loss of craniofacial osteogenic function in mice warrants further study, including investigation using alternative Cre drivers to target different developmental stages of the neural crest. Despite these discrepancies, it is notable that many of the phenotypes we observed after loss of *Eed* in the neural crest of mice were similar to previously reported phenotypes after loss of *Ezh2* in the neural crest cell in mice, with the exception of proliferation deficits after loss of *Eed* but not after loss of *Ezh2* (Ferguson et al., 2018; Schwarz et al., 2014).

Methods

Mice

Mice were maintained in the University of California San Francisco (UCSF) pathogen-free animal facility in accordance with the guidelines established by the Institutional Animal Care and Use Committee (IACUC) and Laboratory Animal Resource Center (LARC) protocol AN191840. Mice were maintained in a 70°F, 50% humidity temperature-controlled barrier facilities under a 12-12h light cycle with access to food and water *ad libitum*. *Sox10-Cre* and Eed^{Fl} mice were obtained from the Jackson Laboratory (B6;CBA-Tg(Sox10-cre)1Wdr/J, 025807 and B6;129S1-Eed^{tm1Sho}/J, 022727, respectively). The presence of the floxed *Eed* allele was determined through standard PCR genotyping using the following primers: 5' GGGACGTGCTGACATTTTCT 3' (forward) and 5' CTTGGGTGGTTTGGCTAAGA 3' (reverse). To generate embryos at specific time points, $Sox10\text{-}Cre^{tg+}$ $Eed^{Fl/WT}$ mice were bred overnight with $Eed^{Fl/Fl}$ *mice.* Females were checked for copulation plugs in the morning and the presence of a vaginal plug was designated as E0.5.

Mouse fetal echocardiography

Ultrasound studies were acquired with a Fujifilm Vevo 2100 Imaging system, and instrument specifically designed for lab animal imaging studies. Pregnant females were anesthetized using an isoflurane/oxygen mixture with an isoflurane concentration of 3% during imaging. The pregnancy date (at least p17) was checked to observe the correct development of fetal hearts. Isoflurane was increased until 5% and the abdomen of pregnant females was open surgically to expose the gravid uterus. The number of fetuses was counted, and craniofacial architecture was evaluated for phenotypic confirmation. Once each fetus was defined as mutant or wild type, echocardiography was performed to evaluate left ventricle anatomy and physiology, including left ventricle size and contractility. Three different measurements were obtained in B and M modes, and functional parameters, including heart rate, fraction shortening, ejection fraction, and left ventricle mass were obtained.

Whole-mount embryo staining

Embryos were stained as previously described (Sandell et al., 2018). In brief, embryos were harvested, and heads were fixed overnight in 4% PFA. Embryos were dehydrated through a methanol series up to 100% before being treated with Dent's bleach (4:1:1, MeOH, DMSO, 30% H2O2) for 2hr at 25°C. Embryos were serially rehydrated in methanol up to 25%, washed with PBST, and stained with DAPI solution (1:40,000, Thermo Scientific, cat# 62248) overnight at 4°C. Samples were mounted in low melt agarose for imaging.

Whole-mount skeletal staining

Embryos were stained as previously described (Rigueur and Lyons, 2013). In brief, embryos were dissected in cold PBS and scalded in hot water to facilitate the removal of eyes, skin, and internal organs. Embryos were fixed in 95% ethanol overnight then subsequently incubated in acetone overnight. Embryos were stained with Alcian Blue solution (Newcomer Supply, cat# 1300B) for 8hr, washed in 70% ethanol, and destained in 95% ethanol. Embryos were cleared in 95% ethanol and 1% KOH, and stained in Alizarin red S solution (SCBT, cat#130-22-3) for 4hr. Embryos were stored in glycerol for imaging.

Micro-computed tomography (microCT)

microCT studies were acquired with a Perkin Elmer´s Quantum GX2 microCT Imaging system, an instrument specifically designed for lab animal imaging studies. The samples were imaged in Eppendorf tubes containing preservative media, which were placed on the scanning bed and fixed with tape to minimize movement. Acquisition parameters were set as follows: FOV 10mm, acquisition time 14 minutes, current voltage 70KV, amperage 114uA. Each study was composed by a 512x512x512 voxels matrix with a spatial resolution of $0.018mm^3$. Study reconstruction was based on Feldkamp´s method using instrument dedicated

software. For image analysis, tridimensional renders were obtained using 3D SLICER software. The threshold range applied for bone segmentation was 300-1400 Hounsfield Units. For the segmentation and visualization of individual frontal bones, cranial base, and mandible, Avizo Lite software (v9.1.1) was used. The threshold range applied was 570-1570 Hounsfield Units.

Cryosectioning and H&E staining

Embryos were fixed in 4% PFA overnight at 4°C and subjected to a sucrose gradient from 15% to 30% before embedding in OCT (Tissue-Tek, cat#4583) and storage at -80°C. Embryos were sectioned at 25µm on a Leica CM1850 cryostat. Slides were immediately subjected to H&E staining as previously described (Cardiff et al., 2014), or stored at -80°C for immunofluorescence.

Immunofluorescence

Immunofluorescence of cryosections was performed on glass slides. Immunofluorescence for primary cells was performed on glass cover slips. Primary cells were fixed in 4% PFA for 10 minutes at room temperature. Antibody incubations were performed in blocking solution (0.1% Triton X-100, 1% BSA, 10% donkey serum) for 2hr at room temperature or overnight at 4°C. Slides or cover slips were mounted in ProLong Diamond Antifade Mountant (Thermo Scientific, cat# P36965). Primary antibodies used in this study were anti-Sox9 (1:500, Proteintech, cat# 67439-1-Ig), anti-Sox9 (1:500, Abcam, cat# ab185230), anti-Runx2 (1:500, Cell Signaling, cat# D1L7F), anti-Ki67 (1:2000, Abcam, cat# ab15580), anti-Vimentin (1:1000, Abcam, cat# ab8069), anti-BrdU (1:1000, Abcam, cat# ab6326), anti-Sox10 (1:500, Cell Signaling, cat# D5V9L), anti-ALPL (1:1000, Invitrogen, cat# PA5-47419), anti-Eed (1:1000, Cell Signaling, cat# E4L6E), and anti-Cleaved Caspase-3 (Asp175) (1:500, Cell Signaling, cat#9661). Secondary antibodies used in this study were Donkey anti-Rabbit IgG (H+L) Alexa Fluor Plus 555 (1:1000, Thermo Scientific, cat# A32794), Donkey anti-Rabbit IgG (H+L) Alexa Fluor 488 (1:1000, Thermo Scientific, cat# A21206), and Donkey anti-Rabbit IgG (H+L) Alexa Fluor Plus 568 (1:1000, Thermo Scientific, cat# A10042). DAPI solution (1:5000, Thermo Scientific, cat# 62248) was added to secondary antibody solutions. Slides or cover slips were mounted in ProLong Diamond Antifade Mountant (Thermo Scientific, cat# P36965) and cured overnight before imaging.

BrdU staining

Timed mating dams were subjected to intraperitoneal injection of 100mg/kg sterile BrdU in PBS (Abcam, cat# ab142567). After 4hr, mice were euthanized, and embryos were harvested in cold PBS. Embryos were fixed in 4% PFA overnight at 4°C and cryosectioned. Sections were incubated with 1M HCl for 2hr then 0.1M sodium borate buffer for 15min before being subjected to standard immunofluorescence.

Microscopy and image analysis

Whole-mount skeletal and H&E stains were imaged using a Zeiss Stemi 305 Stereo Zoom microscope running Zeiss Blue v2.0. Whole-mount embryo DAPI stains were imaged using an upright Zeiss Axio Imager Z2 running AxioVision v4.0. Immunofluorescence images were obtained using a Zeiss LSM800 confocal laser scanning microscope running Zen Blue v2.0. Quantification of embryo measurements and immunofluorescence staining intensities was performed in ImageJ using standard thresholding and measurement of signal integrated density. Signal to nuclei normalization was performed by dividing signal intensity by DAPI signal per image. Quantification was performed using n>6 images per embryo. Proliferation index was calculated by dividing the number of Ki67+ or BrdU+ nuclei by the total number of DAPI stained nuclei per image.

Primary craniofacial cell culture

Timed mating embryos were dissected on ice cold PBS and heads were removed. Brains and eyes were removed from each head, and the remaining craniofacial structures were minced with a sterile blade on a glass surface. Tissue was enzymatically dissociated in 3mg/ml Collagenase Type 7 (Worthington, cat# CLS-6) in HBSS for 2-3hr at 37°C with frequent trituration using an Eppendorf ThermoMixer. Dissociated cells were filtered through a 70uM MACS smart strainer (Miltenyi Biotec, cat#130-110-916) and either plated on cover slips or cell culture dishes. Primary craniofacial cells were grown in DMEM with 10% FBS. For RNA extraction and immunofluorescence, cells were harvested one day following initial dissociation.

Single cell RNA-seq

Matched littermate timed embryos were dissected on ice cold PBS. Embryo heads were removed and minced using sterile razor blades on a glass surface. Tissue was enzymatically dissociated in 3mg/ml

Collagenase Type 7 (Worthington, cat# CLS-6) in HBSS for 2-3hr at 37°C with frequent trituration using an Eppendorf ThermoMixer. The quality of the dissociation was frequently monitored by looking at the cell suspension on an automated cell counter. Cells were spun down at 350rcf, resuspended in MACS BSA stock solution (Miltenyi Biotec, cat# 130-091-376), and serially filtered through 70µm and 40µm MACS smart strainers (Miltenyi Biotec, cat# 130-110-916). Dissociation quality checks, cell viability, and counting was performed using an Invitrogen Countess 3 automated cell counter. 10,000 cells were loaded per single-cell RNA sequencing sample. Single-cell RNA sequencing libraries were generated using the Chromium Single Cell 3' Library & Gel Bead Kit v3.1 on a 10x Genomics Chromium controller using the manufacturer recommended default protocol and settings.

Single-cell RNA sequencing analysis

Library demultiplexing, read alignment to the mouse reference genome mm10, and unique molecular identifier (UMI) quantification was performed in Cell Ranger v7.2.0. Cells with greater than 200 unique genes were retained for analysis. Data were normalized and variance stabilized by SCTransform in Seurat v5.0 (Hao et al., 2024). UMAP and cluster analysis were performed using the Seurat function RunUMAP with parameters of mindist=0.7, res=0.4, dims=1:30. Cluster markers were identified using Seurat function FindAllMarkers with parameters min.pct = 0.25, thresh.use = 0.25. Differential gene expression analysis was performed using DElegate v1.1.0 (Hafemeister and Halbritter, 2023) using the DEseq2 method, with biological replicate animals (n=3 per genotype) as the replicate_column parameter. Featureplots were generated using SCPubr v1.1.2 (Blanco-Carmona, 2022) and scale bars represent log2 UMI's corrected by SCTransform.

Statistics

All experiments were performed with independent biological replicates and repeated, and statistics were derived from biological replicates. Biological replicates are indicated in each figure panel or figure legend. No statistical methods were used to predetermine sample sizes, but sample sizes in this study are similar or larger to those reported in previous publications. Data distribution was assumed to be normal, but this was not formally tested. Investigators were blinded to conditions during data collection and analysis. Bioinformatic analyses were performed blind to clinical features, outcomes, and molecular characteristics. The samples used in this study were nonrandomized with no intervention, and all samples were interrogated equally. Thus, controlling for covariates among samples was not relevant. No data points were excluded from the analyses.

Competing interests statement

The authors declare no competing interests.

Author contributions

All authors made substantial contributions to the conception or design of the study; the acquisition, analysis, or interpretation of data; or drafting or revising the manuscript. All authors approved the manuscript. All authors agree to be personally accountable for individual contributions and to ensure that questions related to the accuracy or integrity of any part of the work are appropriately investigated and resolved and the resolution documented in the literature. T-C.C. and D.R.R. conceived and designed the study. Experiments were performed by T.C-C., C.T., J.A.C.S., and Y-G.J. Data analysis was performed by T.C-C., S.J.L., and D.R.R. S.J.L. performed bioinformatic analyses. The study was supervised by H.N.V., J.O.B., and D.R.R. The manuscript was prepared by T.C-C. and D.R.R. with input from all authors.

Funding

This study was supported by funding from NIH grant T32 CA151022 to T.C-C., NIH grant R35 DE031926 to J.O.B, and NIH grant R21 HD106238 and DOD grant NFRP NF200021 to D.R.R. Sequencing was performed at the UCSF CAT, supported by UCSF PBBR, RRP IMIA, and NIH 1S10OD028511-01 grants.

Data availability

Single-cell RNA sequencing data that were reported in this manuscript have been deposited in the NCBI Sequence Read Archive under PRJNA1077750 (https://www.ncbi.nlm.nih.gov/bioproject/PRJNA1077750).

Code availability

No custom software, tools, or packages were used. The open-source software, tools, and packages used for data analysis in this study are referenced in the methods where applicable and include Cell Ranger v7.2.0, Seurat v5.0, DElegate v1.1.0, and SCPubr v1.1.2.

References

Bertol JW, Johnston S, Ahmed R, Xie VK, Hubka KM, Cruz L, Nitschke L, Stetsiv M, Goering JP, Nistor P, Lowell S, Hoskens H, Claes P, Weinberg SM, Saadi I, Farach-Carson MC, Fakhouri WD. 2022. Twist1 interacts with beta/delta-Catenins during neural tube development and regulates fate transition in cranial neural crest cells. *Development* **149**. doi:10.1242/dev.200068

Blanco-Carmona E. 2022. Generating publication ready visualizations for Single Cell transcriptomics using SCpubr. *bioRxiv* 2022.02.28.482303. doi:10.1101/2022.02.28.482303

Bonnard C, Strobl AC, Shboul M, Lee H, Merriman B, Nelson SF, Ababneh OH, Uz E, Güran T, Kayserili H, Hamamy H, Reversade B. 2012. Mutations in IRX5 impair craniofacial development and germ cell migration via SDF1. *Nat Genet* **44**:709–713. doi:10.1038/ng.2259

Bronner ME, LeDouarin NM. 2012. Development and evolution of the neural crest: An overview. *Dev Biol* **366**:2–9. doi:10.1016/j.ydbio.2011.12.042

Cain CJ, Gaborit N, Lwin W, Barruet E, Ho S, Bonnard C, Hamamy H, Shboul M, Reversade B, Kayserili H, Bruneau BG, Hsiao EC. 2016. Loss of Iroquois homeobox transcription factors 3 and 5 in osteoblasts disrupts cranial mineralization. *Bone Rep* **5**:86–95. doi:10.1016/j.bonr.2016.02.005

Cardiff RD, Miller CH, Munn RJ. 2014. Manual Hematoxylin and Eosin Staining of Mouse Tissue Sections. *Cold Spring Harb Protoc* **2014**:pdb.prot073411. doi:10.1101/pdb.prot073411

Cheung M, Chaboissier M-C, Mynett A, Hirst E, Schedl A, Briscoe J. 2005. The Transcriptional Control of Trunk Neural Crest Induction, Survival, and Delamination. *Dev Cell* **8**:179–192. doi:10.1016/j.devcel.2004.12.010

Cho KY, Kelley BP, Monier D, Lee B, Szabo-Rogers H, Napierala D. 2019. Trps1 Regulates Development of Craniofacial Skeleton and Is Required for the Initiation of Palatal Shelves Fusion. *Front Physiol* **10**:513. doi:10.3389/fphys.2019.00513

Cohen AS, Gibson WT. 2016. EED-associated overgrowth in a second male patient. *J Hum Genet* **61**:831–834. doi:10.1038/jhg.2016.51

Cohen ASA, Tuysuz B, Shen Y, Bhalla SK, Jones SJM, Gibson WT. 2015. A novel mutation in EED associated with overgrowth. *J Hum Genet* **60**:339–342. doi:10.1038/jhg.2015.26

Crispino G, Pasquale GD, Scimemi P, Rodriguez L, Ramirez FG, Siati RDD, Santarelli RM, Arslan E, Bortolozzi M, Chiorini JA, Mammano F. 2011. BAAV Mediated GJB2 Gene Transfer Restores Gap Junction Coupling in Cochlear Organotypic Cultures from Deaf Cx26Sox10Cre Mice. *PLoS ONE* **6**:e23279. doi:10.1371/journal.pone.0023279

Denisenko O, Shnyreva M, Suzuki H, Bomsztyk K. 1998. Point Mutations in the WD40 Domain of Eed Block Its Interaction with Ezh2. *Mol Cell Biol* **18**:5634–5642. doi:10.1128/mcb.18.10.5634

Dudakovic A, Camilleri ET, Xu F, Riester SM, McGee-Lawrence ME, Bradley EW, Paradise CR, Lewallen EA, Thaler R, Deyle DR, Larson AN, Lewallen DG, Dietz AB, Stein GS, Montecino MA, Westendorf JJ, Wijnen AJ van. 2015. Epigenetic Control of Skeletal Development by the Histone Methyltransferase Ezh2*. *J Biol Chem* **290**:27604–27617. doi:10.1074/jbc.m115.672345

Fantauzzo KA, Christiano AM. 2011. Trps1 activates a network of secreted Wnt inhibitors and transcription factors crucial to vibrissa follicle morphogenesis. *Development* **139**:203–214. doi:10.1242/dev.069971

Faust C, Schumacher A, Holdener B, Magnuson T. 1995. The eed mutation disrupts anterior mesoderm production in mice. *Development* **121**:273–285. doi:10.1242/dev.121.2.273

Ferguson JW, Devarajan M, Atit RP. 2018. Stage-specific roles of Ezh2 and Retinoic acid signaling ensure calvarial bone lineage commitment. *Dev Biol* **443**:173–187. doi:10.1016/j.ydbio.2018.09.014

Frisdal A, Trainor PA. 2014. Development and evolution of the pharyngeal apparatus. *Wiley Interdiscip Rev: Dev Biol* **3**:403–418. doi:10.1002/wdev.147

Gao CW, Lin W, Riddle RC, Kushwaha P, Boukas L, Björnsson HT, Hansen KD, Fahrner JA. 2023. Novel mouse model of Weaver syndrome displays overgrowth and excess osteogenesis reversible with KDM6A/6B inhibition. *bioRxiv* 2023.06.23.546270. doi:10.1101/2023.06.23.546270

Gerdes J, Lemke H, Baisch H, Wacker HH, Schwab U, Stein H. 1984. Cell cycle analysis of a cell proliferation-associated human nuclear antigen defined by the monoclonal antibody Ki-67. *J Immunol (Baltim, Md□: 1950)* **133**:1710–5.

Gibson WT, Hood RL, Zhan SH, Bulman DE, Fejes AP, Moore R, Mungall AJ, Eydoux P, Babul-Hirji R, An J, Marra MA, Consortium FC, Chitayat D, Boycott KM, Weaver DD, Jones SJM. 2012. Mutations in EZH2 Cause Weaver Syndrome. *Am J Hum Genet* **90**:110–118. doi:10.1016/j.ajhg.2011.11.018

Goel H, O'Donnell S, Edwards M. 2024. EED related overgrowth: First report of multiple members in a single family. *Am J Méd Genet Part A* **194**:374–382. doi:10.1002/ajmg.a.63438

Hafemeister C, Halbritter F. 2023. Single-cell RNA-seq differential expression tests within a sample should use pseudo-bulk data of pseudo-replicates. *bioRxiv* 2023.03.28.534443. doi:10.1101/2023.03.28.534443

Hao Y, Stuart T, Kowalski MH, Choudhary S, Hoffman P, Hartman A, Srivastava A, Molla G, Madad S, Fernandez-Granda C, Satija R. 2024. Dictionary learning for integrative, multimodal and scalable single-cell analysis. *Nat Biotechnol* **42**:293–304. doi:10.1038/s41587-023-01767-y

Honoré SM, Aybar MJ, Mayor R. 2003. Sox10 is required for the early development of the prospective neural crest in Xenopus embryos. *Dev Biol* **260**:79–96. doi:10.1016/s0012-1606(03)00247-1

Ianevski A, Giri AK, Aittokallio T. 2022. Fully-automated and ultra-fast cell-type identification using specific marker combinations from single-cell transcriptomic data. *Nat Commun* **13**:1246. doi:10.1038/s41467-022-28803-w

Imagawa E, Albuquerque EVA, Isidor B, Mitsuhashi S, Mizuguchi T, Miyatake S, Takata A, Miyake N, Boguszewski MCS, Boguszewski CL, Lerario AM, Funari MA, Jorge AAL, Matsumoto N. 2018. Novel SUZ12 mutations in Weaver-like syndrome. *Clin Genet* **94**:461–466. doi:10.1111/cge.13415

Jang YO, Cho M-Y, Yun C-O, Baik SK, Park K-S, Cha S-K, Chang SJ, Kim MY, Lim YL, Kwon SO. 2016. Effect of Function-Enhanced Mesenchymal Stem Cells Infected With Decorin-Expressing Adenovirus on Hepatic Fibrosis. *Stem Cells Transl Med* **5**:1247–1256. doi:10.5966/sctm.2015-0323

Jeong J, Mao J, Tenzen T, Kottmann AH, McMahon AP. 2004. Hedgehog signaling in the neural crest cells regulates the patterning and growth of facial primordia. *Genes Dev* **18**:937–951. doi:10.1101/gad.1190304

Jing H, Liao L, An Y, Su X, Liu S, Shuai Y, Zhang X, Jin Y. 2016. Suppression of EZH2 Prevents the Shift of Osteoporotic MSC Fate to Adipocyte and Enhances Bone Formation During Osteoporosis. *Mol Ther* **24**:217–229. doi:10.1038/mt.2015.152

Kawane T, Qin X, Jiang Q, Miyazaki T, Komori H, Yoshida CA, Matsuura-Kawata VK dos S, Sakane C, Matsuo Y, Nagai K, Maeno T, Date Y, Nishimura R, Komori T. 2018. Runx2 is required for the proliferation of osteoblast progenitors and induces proliferation by regulating Fgfr2 and Fgfr3. *Sci Rep* **8**:13551. doi:10.1038/s41598-018-31853-0

Kim H, Langohr IM, Faisal M, McNulty M, Thorn C, Kim J. 2018. Ablation of Ezh2 in neural crest cells leads to aberrant enteric nervous system development in mice. *PLoS ONE* **13**:e0203391. doi:10.1371/journal.pone.0203391

Kim J, Lo L, Dormand E, Anderson DJ. 2003. SOX10 Maintains Multipotency and Inhibits Neuronal Differentiation of Neural Crest Stem Cells. *Neuron* **38**:17–31. doi:10.1016/s0896-6273(03)00163-6

Kim SY, Paylor SW, Magnuson T, Schumacher A. 2006. Juxtaposed Polycomb complexes co-regulate vertebral identity. *Development* **133**:4957–4968. doi:10.1242/dev.02677

Komori T. 2009. Osteoimmunology, Interactions of the Immune and skeletal systems II. *Adv Exp Med Biol* **658**:43–49. doi:10.1007/978-1-4419-1050-9_5

Lamandé SR, Mörgelin M, Adams NE, Selan C, Allen JM. 2006. The C5 domain of the collagen VI alpha3(VI) chain is critical for extracellular microfibril formation and is present in the extracellular matrix of cultured cells. *J Biol Chem* **281**:16607–14. doi:10.1074/jbc.m510192200

Lee MS, Lowe G, Flanagan S, Kuchler K, Glackin CA. 2000. Human dermo-1 has attributes similar to twist in early bone development. *Bone* **27**:591–602. doi:10.1016/s8756-3282(00)00380-x

Lindsay EA, Botta A, Jurecic V, Carattini-Rivera S, Cheah Y-C, Rosenblatt HM, Bradley A, Baldini A. 1999. Congenital heart disease in mice deficient for the DiGeorge syndrome region. *Nature* **401**:379–383. doi:10.1038/43900

Lindsay EA, Vitelli F, Su H, Morishima M, Huynh T, Pramparo T, Jurecic V, Ogunrinu G, Sutherland HF, Scambler PJ, Bradley A, Baldini A. 2001. Tbx1 haploinsufficiency in the DiGeorge syndrome region causes aortic arch defects in mice. *Nature* **410**:97–101. doi:10.1038/35065105

Liu W, Zhang L, Xuan K, Hu C, Liu S, Liao L, Li B, Jin F, Shi S, Jin Y. 2018. Alpl prevents bone ageing sensitivity by specifically regulating senescence and differentiation in mesenchymal stem cells. *Bone Res* **6**:27. doi:10.1038/s41413-018-0029-4

Liu Y, Strecker S, Wang L, Kronenberg MS, Wang W, Rowe DW, Maye P. 2013. Osterix-Cre Labeled Progenitor Cells Contribute to the Formation and Maintenance of the Bone Marrow Stroma. *PLoS ONE* **8**:e71318. doi:10.1371/journal.pone.0071318

Luo Lin, Ambrozkiewicz MC, Benseler F, Chen C, Dumontier E, Falkner S, Furlanis E, Gomez AM, Hoshina N, Huang W-H, Hutchison MA, Itoh-Maruoka Y, Lavery LA, Li W, Maruo T, Motohashi J, Pai EL-L, Pelkey KA, Pereira A, Philips T, Sinclair JL, Stogsdill JA, Traunmüller L, Wang J, Wortel J, You W, Abumaria N, Beier KT, Brose N, Burgess HA, Cepko CL, Cloutier J-F, Eroglu C, Goebbels S, Kaeser PS, Kay JN, Lu W, Luo Liqun, Mandai K, McBain CJ, Nave K-A, Prado MAM, Prado VF, Rothstein J, Rubenstein JLR, Saher G, Sakimura K, Sanes JR, Scheiffele P, Takai Y, Umemori H, Verhage M, Yuzaki M, Zoghbi HY, Kawabe H, Craig AM. 2020. Optimizing Nervous System-Specific Gene Targeting with Cre Driver Lines: Prevalence of Germline Recombination and Influencing Factors. *Neuron* **106**:37-65.e5. doi:10.1016/j.neuron.2020.01.008

Maczkowiak F, Matéos S, Wang E, Roche D, Harland R, Monsoro-Burq AH. 2010. The Pax3 and Pax7 paralogs cooperate in neural and neural crest patterning using distinct molecular mechanisms, in Xenopus laevis embryos. *Dev Biol* **340**:381–396. doi:10.1016/j.ydbio.2010.01.022

Margueron R, Reinberg D. 2011. The Polycomb complex PRC2 and its mark in life. *Nature* **469**:343–349. doi:10.1038/nature09784

Matsuoka T, Ahlberg PE, Kessaris N, Iannarelli P, Dennehy U, Richardson WD, McMahon AP, Koentges G. 2004. Neural crest origins of the neck and shoulder. *Nature* **436**:347–55. doi:10.1038/nature03837

Mendez MG, Kojima S, Goldman RD. 2010. Vimentin induces changes in cell shape, motility, and adhesion during the epithelial to mesenchymal transition. *FASEB J* **24**:1838–1851. doi:10.1096/fj.09-151639

Metzis V, Courtney AD, Kerr MC, Ferguson C, Galeano MCR, Parton RG, Wainwright BJ, Wicking C. 2013. Patched1 is required in neural crest cells for the prevention of orofacial clefts. *Hum Mol Genet* **22**:5026–5035. doi:10.1093/hmg/ddt353

Minoux M, Rijli FM. 2010. Molecular mechanisms of cranial neural crest cell migration and patterning in craniofacial development. *Development* **137**:2605–2621. doi:10.1242/dev.040048

Mirzamohammadi F, Papaioannou G, Inloes JB, Rankin EB, Xie H, Schipani E, Orkin SH, Kobayashi T. 2016. Polycomb repressive complex 2 regulates skeletal growth by suppressing Wnt and TGF-β signalling. *Nat Commun* **7**:12047. doi:10.1038/ncomms12047

Montgomery ND, Yee D, Montgomery SA, Magnuson T. 2007. Molecular and Functional Mapping of EED Motifs Required for PRC2-Dependent Histone Methylation. *J Mol Biol* **374**:1145–1157. doi:10.1016/j.jmb.2007.10.040

Mori-Akiyama Y, Akiyama H, Rowitch DH, Crombrugghe B de. 2003. Sox9 is required for determination of the chondrogenic cell lineage in the cranial neural crest. *Proc Natl Acad Sci* **100**:9360–9365. doi:10.1073/pnas.1631288100

Nakamura T, Gulick J, Colbert MC, Robbins J. 2009. Protein tyrosine phosphatase activity in the neural crest is essential for normal heart and skull development. *Proc Natl Acad Sci* **106**:11270–11275. doi:10.1073/pnas.0902230106

Niethamer TK, Teng T, Franco M, Du YX, Percival CJ, Bush JO. 2020. Aberrant cell segregation in the craniofacial primordium and the emergence of facial dysmorphology in craniofrontonasal syndrome. *PLoS Genet* **16**:e1008300. doi:10.1371/journal.pgen.1008300

O'Carroll D, Erhardt S, Pagani M, Barton SC, Surani MA, Jenuwein T. 2001. The polycomb-group gene Ezh2 is required for early mouse development. *Mol Cell Biol* **21**:4330–6. doi:10.1128/mcb.21.13.4330-4336.2001

Pasini D, Bracken AP, Jensen MR, Denchi EL, Helin K. 2004. Suz12 is essential for mouse development and for EZH2 histone methyltransferase activity. *EMBO J* **23**:4061–4071. doi:10.1038/sj.emboj.7600402

Piunti A, Shilatifard A. 2021. The roles of Polycomb repressive complexes in mammalian development and cancer. *Nat Rev Mol Cell Biol* **22**:326–345. doi:10.1038/s41580-021-00341-1

Rigueur D, Lyons KM. 2013. Skeletal Development and Repair, Methods and Protocols. *Methods Mol Biol* **1130**:113–121. doi:10.1007/978-1-62703-989-5_9

Rotllant J, Liu D, Yan Y-L, Postlethwait JH, Westerfield M, Du S-J. 2008. Sparc (Osteonectin) functions in morphogenesis of the pharyngeal skeleton and inner ear. *Matrix Biol* **27**:561–572. doi:10.1016/j.matbio.2008.03.001

Sandell L, Inman K, Trainor P. 2018. DAPI Staining of Whole-Mount Mouse Embryos or Fetal Organs. *Cold Spring Harb Protoc* **2018**:pdb.prot094029. doi:10.1101/pdb.prot094029

Schumacher A, Faust C, Magnuson T. 1996. Positional cloning of a global regulator of anterior–posterior patterning in mice. *Nature* **383**:250–253. doi:10.1038/383250a0

Schwarz D, Varum S, Zemke M, Schöler A, Baggiolini A, Draganova K, Koseki H, Schübeler D, Sommer L. 2014. Ezh2 is required for neural crest-derived cartilage and bone formation. *Development* **141**:867–877. doi:10.1242/dev.094342

Shukunami C, Takimoto A, Oro M, Hiraki Y. 2006. Scleraxis positively regulates the expression of tenomodulin, a differentiation marker of tenocytes. *Dev Biol* **298**:234–247. doi:10.1016/j.ydbio.2006.06.036

Shull LC, Sen R, Menzel J, Goyama S, Kurokawa M, Artinger KB. 2020. The conserved and divergent roles of Prdm3 and Prdm16 in zebrafish and mouse craniofacial development. *Dev Biol* **461**:132–144. doi:10.1016/j.ydbio.2020.02.006

Simões-Costa M, Bronner ME. 2015. Establishing neural crest identity: a gene regulatory recipe. *Development* **142**:242–257. doi:10.1242/dev.105445

Smits P, Li P, Mandel J, Zhang Z, Deng JM, Behringer RR, Crombrugghe B de, Lefebvre V. 2001. The Transcription Factors L-Sox5 and Sox6 Are Essential for Cartilage Formation. *Dev Cell* **1**:277–290. doi:10.1016/s1534-5807(01)00003-x

Spellicy CJ, Peng Y, Olewiler L, Cathey SS, Rogers RC, Bartholomew D, Johnson J, Alexov E, Lee JA, Friez MJ, Jones JR. 2019. Three additional patients with EED-associated overgrowth: potential mutation hotspots identified? *J Hum Genet* **64**:561–572. doi:10.1038/s10038-019-0585-5

Tamamura Y, Katsube K, Mera H, Itokazu M, Wakitani S. 2017. Irx3 and Bmp2 regulate mouse mesenchymal cell chondrogenic differentiation in both a Sox9-dependent and -independent manner. *J Cell Physiol* **232**:3317–3336. doi:10.1002/jcp.25776

Tan Z, Kong M, Wen S, Tsang KY, Niu B, Hartmann C, Chan D, Hui C, Cheah KSE. 2020. IRX3 and IRX5 Inhibit Adipogenic Differentiation of Hypertrophic Chondrocytes and Promote Osteogenesis. *J Bone Miner Res* **35**:2444–2457. doi:10.1002/jbmr.4132

Tatton-Brown K, Murray A, Hanks S, Douglas J, Armstrong R, Banka S, Bird LM, Clericuzio CL, Cormier-Daire V, Cushing T, Flinter F, Jacquemont M, Joss S, Kinning E, Lynch SA, Magee A, McConnell V, Medeira A, Ozono K, Patton M, Rankin J, Shears D, Simon M, Splitt M, Strenger V, Stuurman K, Taylor C, Titheradge H, Maldergem LV, Temple IK, Cole T, Seal S, Consortium CO, Rahman N. 2013. Weaver syndrome and EZH2 mutations: Clarifying the clinical phenotype. *Am J Méd Genet Part A* **161**:2972–2980. doi:10.1002/ajmg.a.36229

Tien C-L, Jones A, Wang H, Gerigk M, Nozell S, Chang C. 2015. Snail2/Slug cooperates with Polycomb repressive complex 2 (PRC2) to regulate neural crest development. *Development* **142**:722–731. doi:10.1242/dev.111997

Yan Y-L, Miller CT, Nissen RM, Singer A, Liu D, Kirn A, Draper B, Willoughby J, Morcos PA, Amsterdam A, Chung B-C, Westerfield M, Haffter P, Hopkins N, Kimmel C, Postlethwait JH, Nissen R. 2002. A zebrafish sox9 gene required for cartilage morphogenesis. *Dev (Camb, Engl)* **129**:5065–79. doi:10.1242/dev.129.21.5065

Yu M, Riva L, Xie H, Schindler Y, Moran TB, Cheng Y, Yu D, Hardison R, Weiss MJ, Orkin SH, Bernstein BE, Fraenkel E, Cantor AB. 2009. Insights into GATA-1-Mediated Gene Activation versus Repression via Genome-wide Chromatin Occupancy Analysis. *Mol Cell* **36**:682–695. doi:10.1016/j.molcel.2009.11.002

Figures

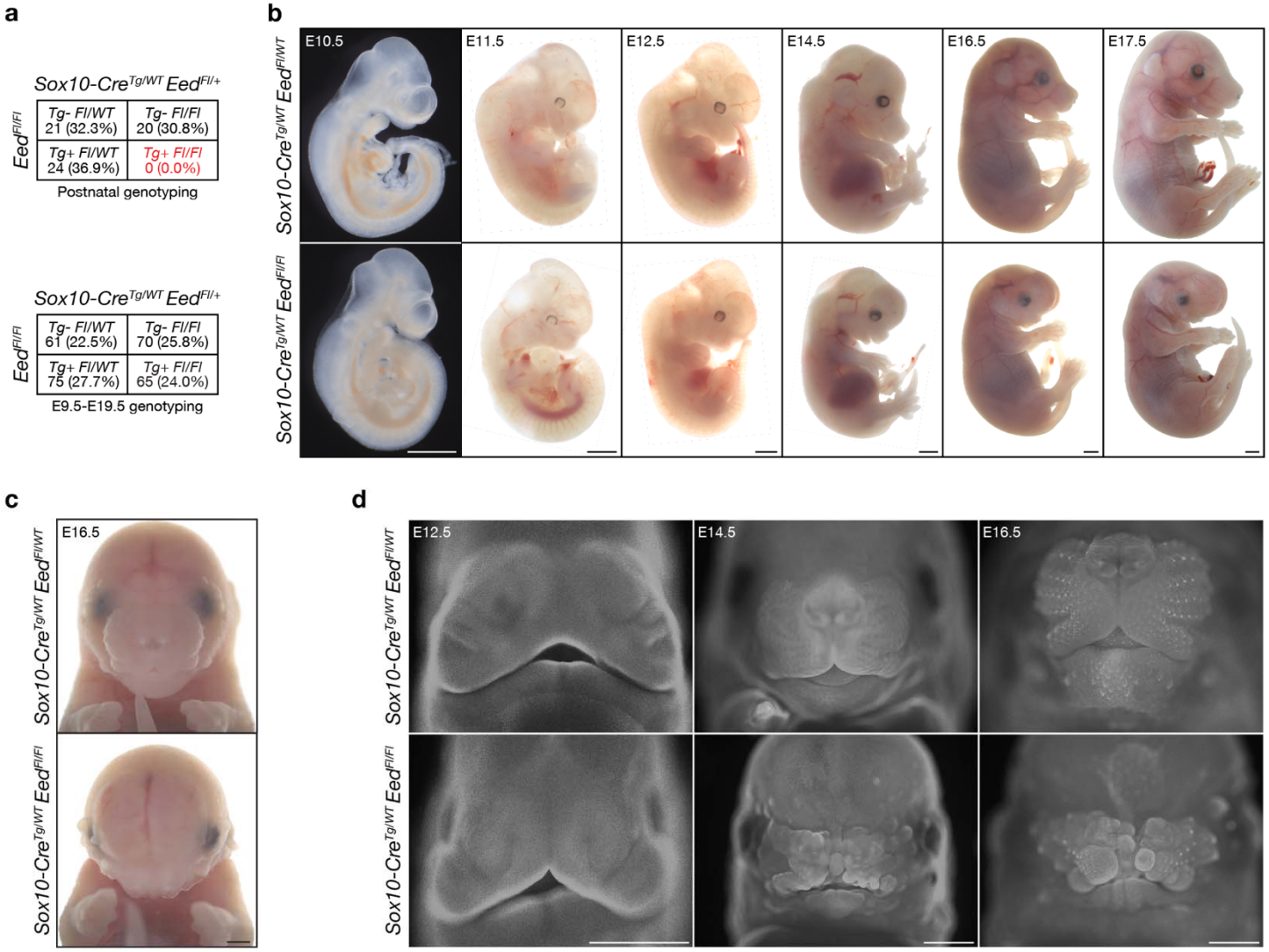

Fig. 1. Sox10-Cre Eed$^{Fl/Fl}$ embryos develop craniofacial malformations. (a) Genotyping frequencies of postnatal (top) and embryonic (bottom) *Sox10-Cre Eed$^{Fl/Fl}$* mice. (b) Sagittal brightfield images of *Sox10-Cre Eed$^{Fl/WT}$* or *Sox10-Cre Eed$^{Fl/Fl}$* embryos from E10.5 to E17.5 showing craniofacial malformations appearing at E12.5 that were observed with 100% penetrance. Scale bar, 1mm. (c) Coronal brightfield images of E16.5 *Sox10-Cre Eed$^{Fl/WT}$* or *Sox10-Cre Eed$^{Fl/Fl}$* embryos showing craniofacial malformations. Scale bar, 1mm. (d) Whole-mount fluorescence microscopy of DAPI-stained *Sox10-Cre Eed$^{Fl/WT}$* or *Sox10-Cre Eed$^{Fl/Fl}$* heads at E12.5, E14.5, or E16.5. Scale bar, 1mm. All images are representative of ≥3 biological replicates.

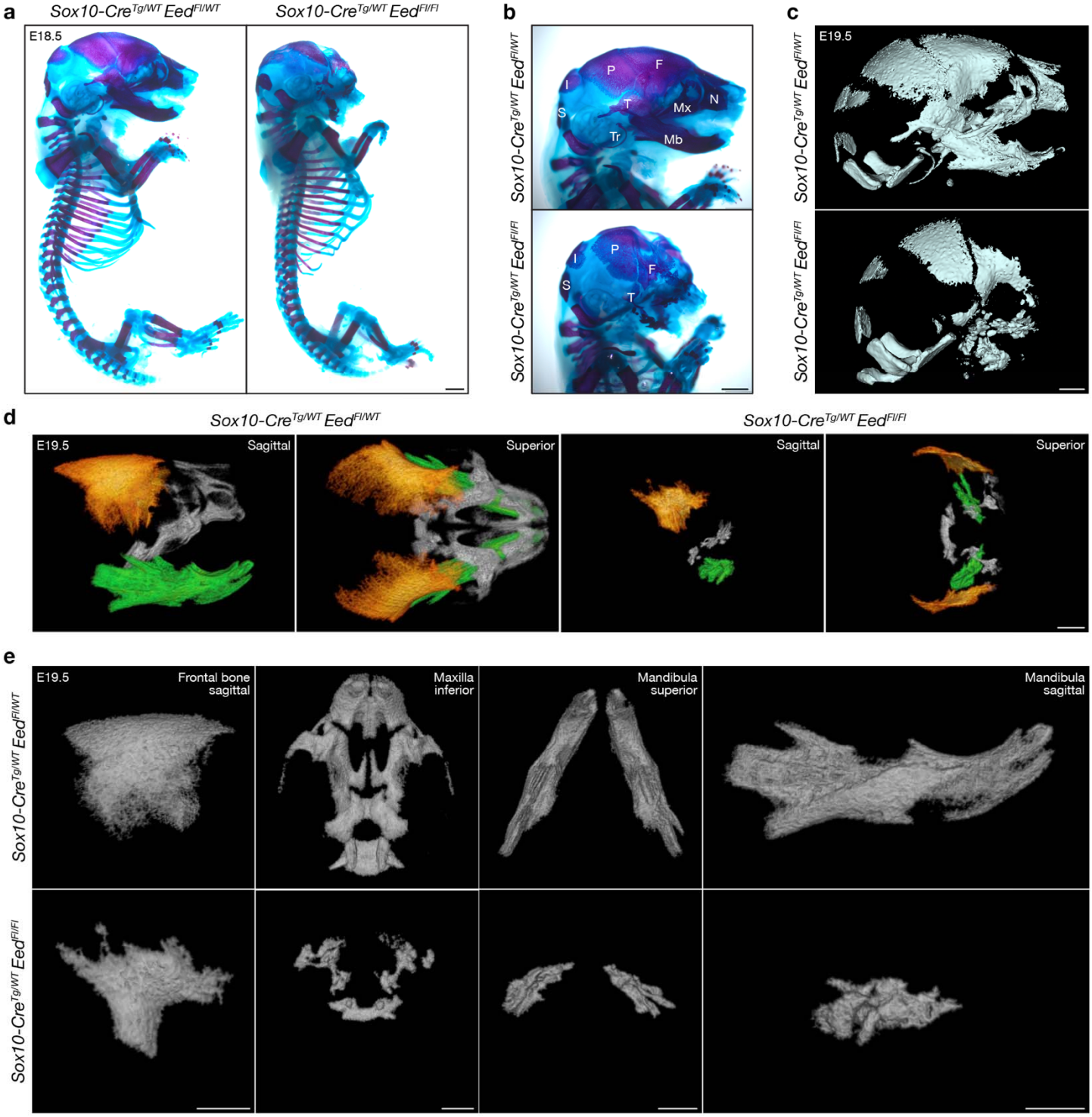

Fig. 2. Eed is required for craniofacial skeletal development from the neural crest. (a) Sagittal brightfield images of whole-mount skeletal stains of E18.5 *Sox10-Cre Eed*$^{Fl/WT}$ or *Sox10-Cre Eed*$^{Fl/Fl}$ embryos. Alcian blue and alizarin red identify cartilage or bone, respectively. Scale bar, 1mm. (b) Magnified sagittal brightfield images of whole-mount skeletal stains of E18.5 *Sox10-Cre Eed*$^{Fl/WT}$ or *Sox10-Cre Eed*$^{Fl/Fl}$ embryos. Bones structures are annotated (I, interparietal; P, parietal; Mx, maxilla; Mb, mandible; Tr, tympanic ring; F, frontal; N, nasal; T, temporal; S, supraoccipital). Scale bar, 1mm. (c) Micro-CT images of E19.5 *Sox10-Cre Eed*$^{Fl/WT}$ or *Sox10-Cre Eed*$^{Fl/Fl}$ heads. Scale bar, 1mm. (d) Micro-CT images of E19.5 *Sox10-Cre Eed*$^{Fl/WT}$ or *Sox10-Cre Eed*$^{Fl/Fl}$ neural crest-derived craniofacial bones shaded in orange (frontal), grey (maxilla), or green (mandible). Scale bar, 1mm. (d) Magnified micro-CT images of E19.5 *Sox10-Cre Eed*$^{Fl/WT}$ or *Sox10-Cre Eed*$^{Fl/Fl}$ neural crest-derived craniofacial bones. Scale bars, 1mm.

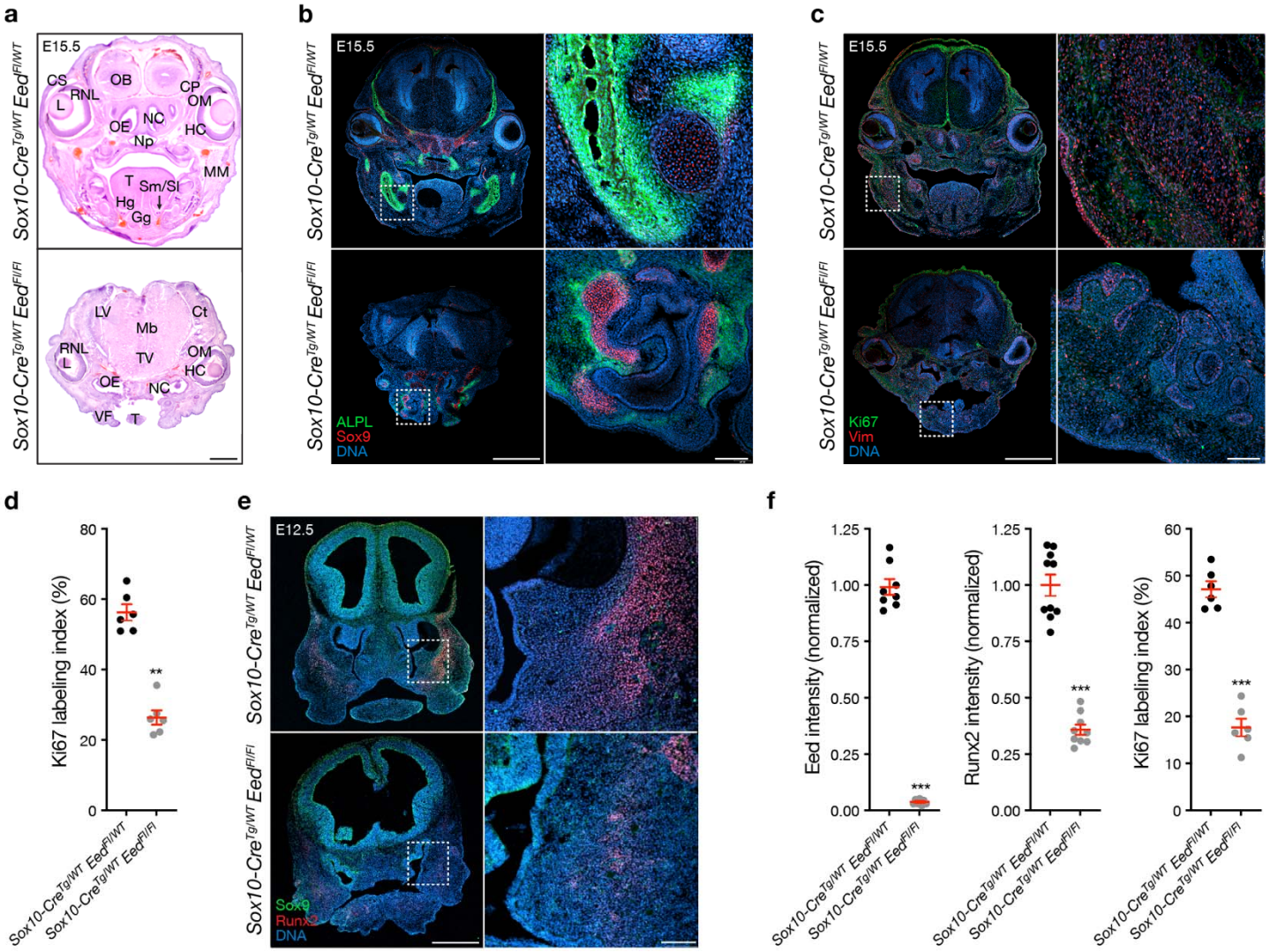

Fig. 3. Eed regulates craniofacial differentiation and proliferation from the neural crest. (a) Brightfield coronal H&E images of E15.5 *Sox10-Cre Eed*$^{Fl/WT}$ or *Sox10-Cre Eed*$^{Fl/Fl}$ heads. Anatomic structures are annotated (Ct, cortex; CP, cartilage primordium; CS, conjunctival sac; Gg, genioglossus muscle; HC, hyaloid cavity; Hg, hyoglossus muscle; L, lens; LV, lateral ventricle; Mb, midbrain; MM, masseter muscle; Np, nasopharynx; NC, nasal cavity; OB, olfactory bulb; OE, olfactory epithelium; OM, ocular muscle; RNL, retina neural layer; Sm/St, sublingual and submandibular ducts; T, tongue; TV, third ventricle; VF, vibrissa follicles). Scale bar, 1mm. (b) Coronal immunofluorescence images of E15.5 *Sox10-Cre Eed*$^{Fl/WT}$ or *Sox10-Cre Eed*$^{Fl/Fl}$ heads stained for ALPL (green) and Sox9 (red). Scale bars, 1mm and 100µm. (c) Coronal immunofluorescence images of E15.5 *Sox10-Cre Eed*$^{Fl/WT}$ or *Sox10-Cre Eed*$^{Fl/Fl}$ heads stained for Ki67 (green) and Vimentin (red). Scale bars, 1mm and 100µm. (d) Quantification of Ki67 immunofluorescence labeling index from E15.5 heads. (e) Coronal immunofluorescence images of E12.5 *Sox10-Cre Eed*$^{Fl/WT}$ or *Sox10-Cre Eed*$^{Fl/Fl}$ heads stained for Runx2 (red) and Sox9 (green). Intracranial tissues demonstrate *ex vacuo* dilation and anterior herniation in *Sox10-Cre Eed*$^{Fl/Fl}$ heads. Scale bars, 500µm and 100µm. (f) Quantification of immunofluorescence imaging intensity from primary craniofacial cell cultures from E12.5 *Sox10-Cre Eed*$^{Fl/WT}$ or *Sox10-Cre Eed*$^{Fl/Fl}$ embryos. All images are representative of ≥3 biological replicates. DNA is marked by DAPI. Lines represent means and error bars represent standard error of the means. Student's t-tests, **$p \leq 0.01$, ***$p \leq 0.0001$.

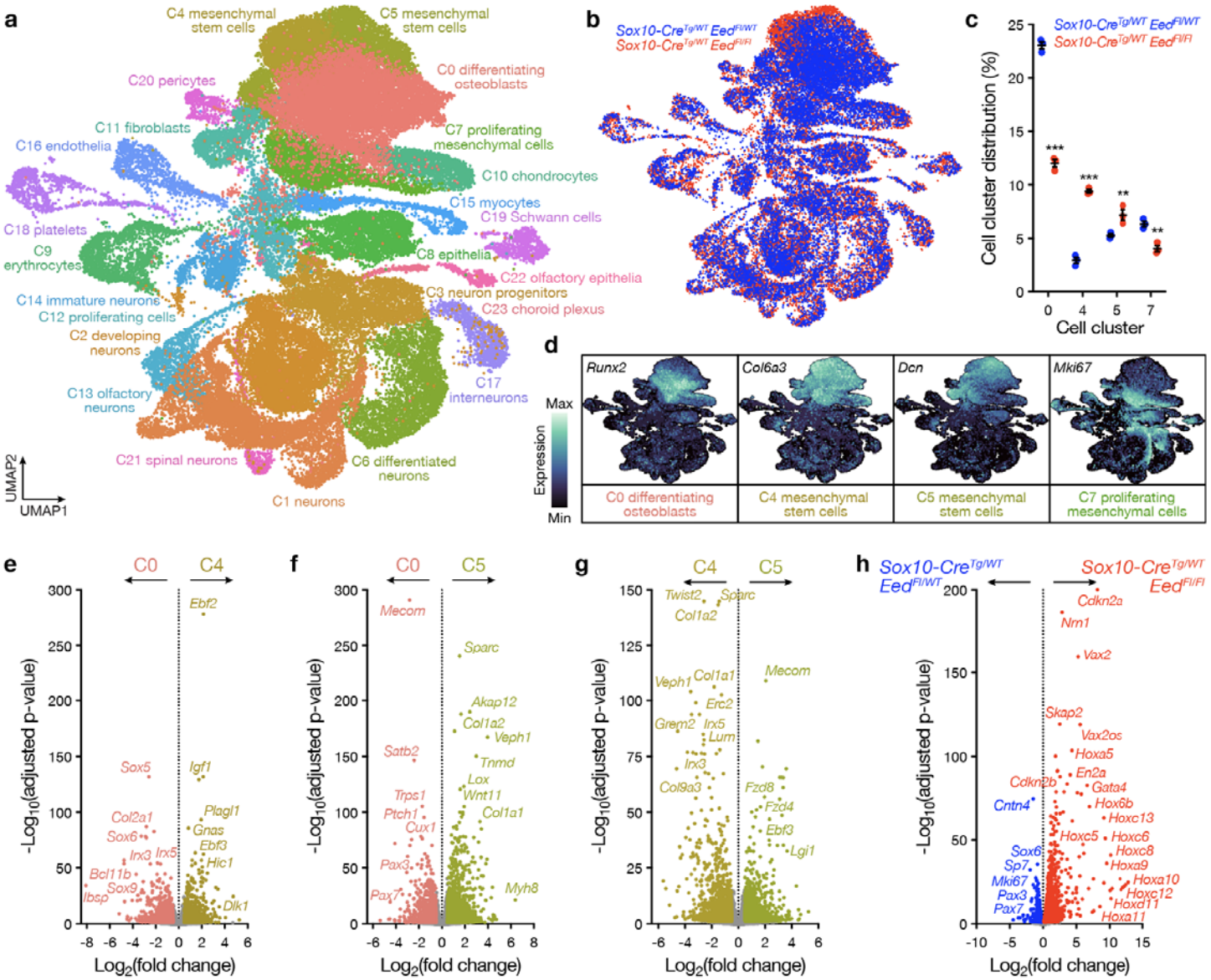

Fig. 4. Eed regulates craniofacial mesenchymal stem cell, osteoblast, and proliferating mesenchymal cell fate from the neural crest. (a) Integrated UMAP of 63,730 transcriptomes from single-cell RNA sequencing of litter-matched E12.5 *Sox10-Cre Eed*$^{Fl/WT}$ (n=3) or *Sox10-Cre Eed*$^{Fl/Fl}$ (n=3) heads. (b) Integrated UMAP overlaying cell cluster distribution from single-cell RNA sequencing. (c) Quantification of mesenchymal cell cluster distribution from single-cell RNA sequencing. Lines represent means and error bars represent standard error of the means. Student's t-tests, **p≤0.01, ***p≤0.0001. (d) Gene expression feature plots of mesenchymal lineages from single-cell RNA sequencing. (e) Volcano plot showing differentially expressed genes between C0 (osteoblasts) and C4 (mesenchymal stem cells). (f) Volcano plot showing differentially expressed genes between C0 and C5 (mesenchymal stem cells). (g) Volcano plot showing differentially expressed genes between 2 clusters of mesenchymal stem cells from single-cell RNA sequencing of litter-matched E12.5 *Sox10-Cre Eed*$^{Fl/WT}$ (n=3) or *Sox10-Cre Eed*$^{Fl/Fl}$ (n=3) heads. (h) Volcano plot showing differentially expressed genes in differentiating osteoblasts (C0), mesenchymal stem cells (C4, C5), and proliferating mesenchymal cells (C7) from single-cell RNA sequencing of litter-matched E12.5 *Sox10-Cre Eed*$^{Fl/WT}$ (n=3) versus *Sox10-Cre Eed*$^{Fl/Fl}$ (n=3) heads.

Supplementary figures

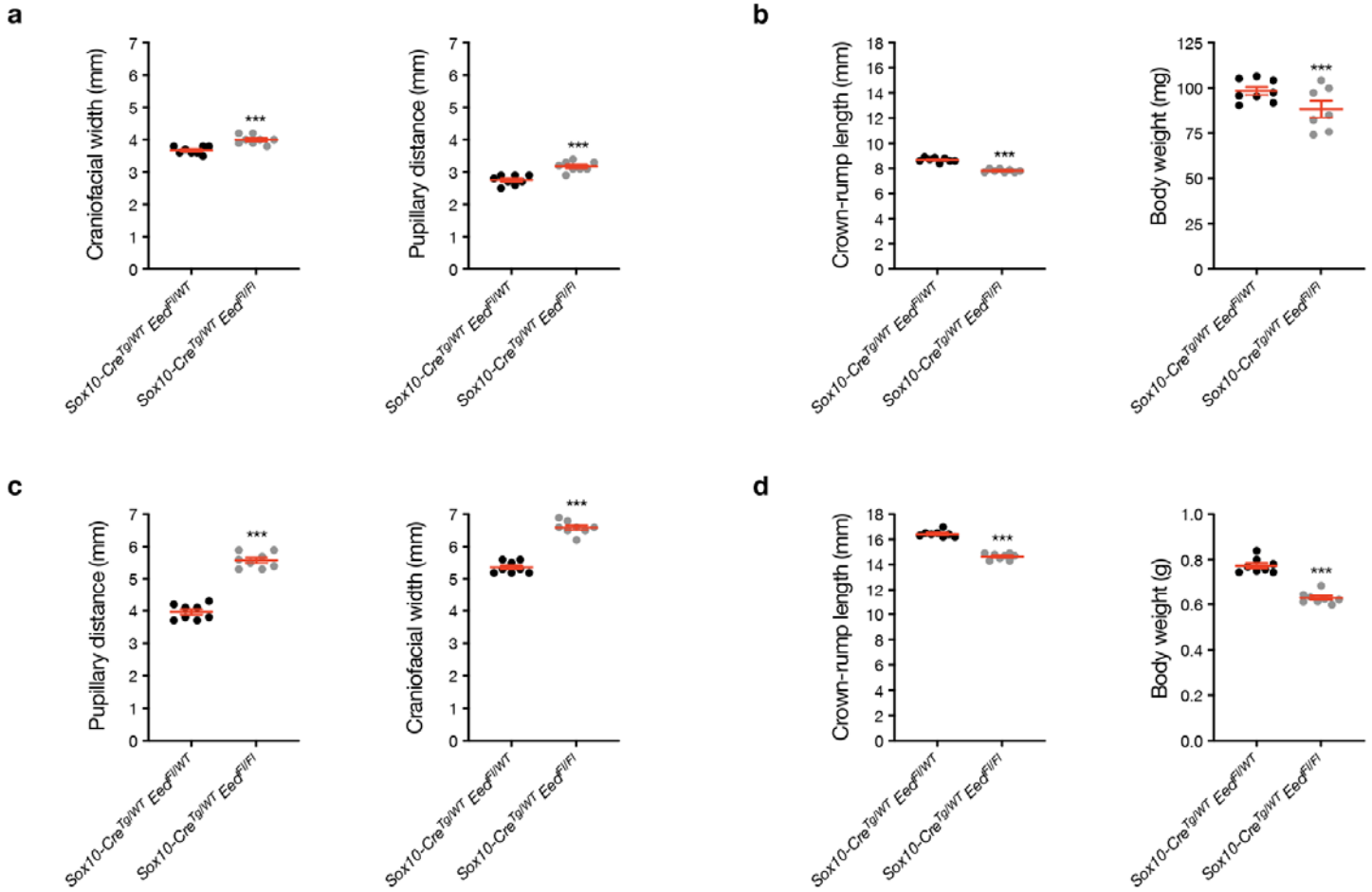

Supplementary Fig. 1. Sox10-Cre Eed$^{Fl/Fl}$ embryos develop craniofacial malformations. (a) Craniofacial measurement quantification of pupillary distance (left) or craniofacial width (right) from E12.5 *Sox10-Cre Eed$^{Fl/WT}$* or *Sox10-Cre Eed$^{Fl/Fl}$* embryos. (b) Body measurement quantification of crown-rump length from E12.5 *Sox10-Cre Eed$^{Fl/WT}$* or *Sox10-Cre Eed$^{Fl/Fl}$* embryos. Lines represent means and error bars represent standard error of the means. (c) Craniofacial measurement quantification of pupillary distance (left) or craniofacial width (right) from E16.5 *Sox10-Cre Eed$^{Fl/WT}$* or *Sox10-Cre Eed$^{Fl/Fl}$* embryos. (d) Body measurement quantification of crown-rump length (left) or body weight (right) from E16.5 *Sox10-Cre Eed$^{Fl/WT}$* or *Sox10-Cre Eed$^{Fl/Fl}$* embryos. Lines represent means and error bars represent standard error of the means. Student's t-tests, ***$p \leq 0.0001$.

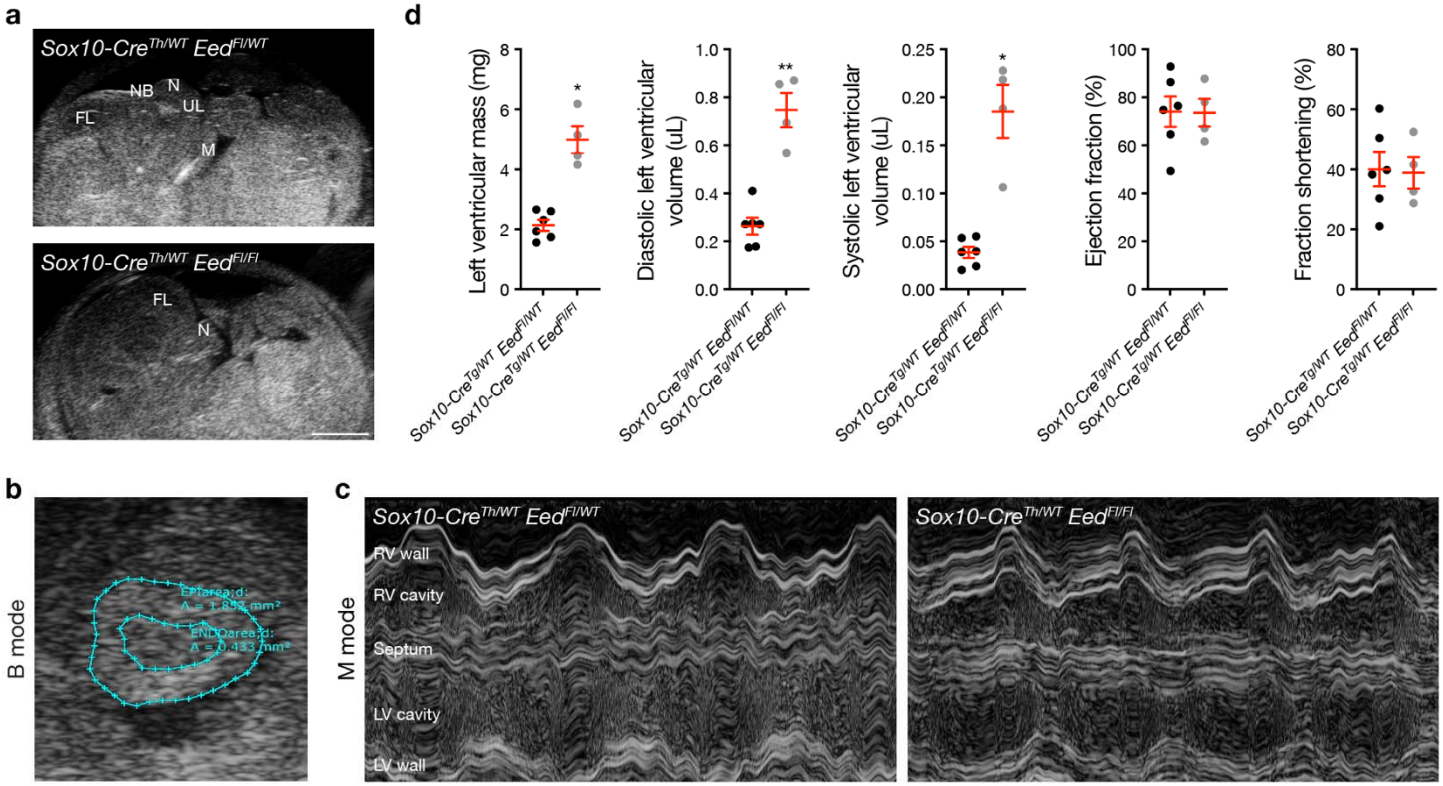

Supplementary Fig. 2. Sox10-Cre Eed$^{Fl/Fl}$ embryos develop subtle cardiac malformations. (a) Sagittal view of E16.5 *Sox10-Cre Eed$^{Fl/WT}$* (top) or *Sox10-Cre Eed$^{Fl/Fl}$* (bottom) embryos in B-mode echocardiography (FL, frontal lobe; NB, nasal bridge; N, nose; UL, upper lip; M, mandible). Scale bar, 1mm. (b) Transversal view of B-mode echocardiography with measurements of left ventricle internal and external areas of an E16.5 embryo. (c) M-mode echocardiography of E16.5 *Sox10-Cre Eed$^{Fl/WT}$* (left) or *Sox10-Cre Eed$^{Fl/Fl}$* (right) embryos. Four cardiac cycles are included per trace and all cardiac segments are visible in each embryo, as labeled. (d) Quantitative echocardiography measurements from *Sox10-Cre Eed$^{Fl/WT}$* or *Sox10-Cre Eed$^{Fl/Fl}$* embryos. Lines represent means and error bars represent standard error of the means. Student's t-tests, *p≤0.05, **p≤0.01.

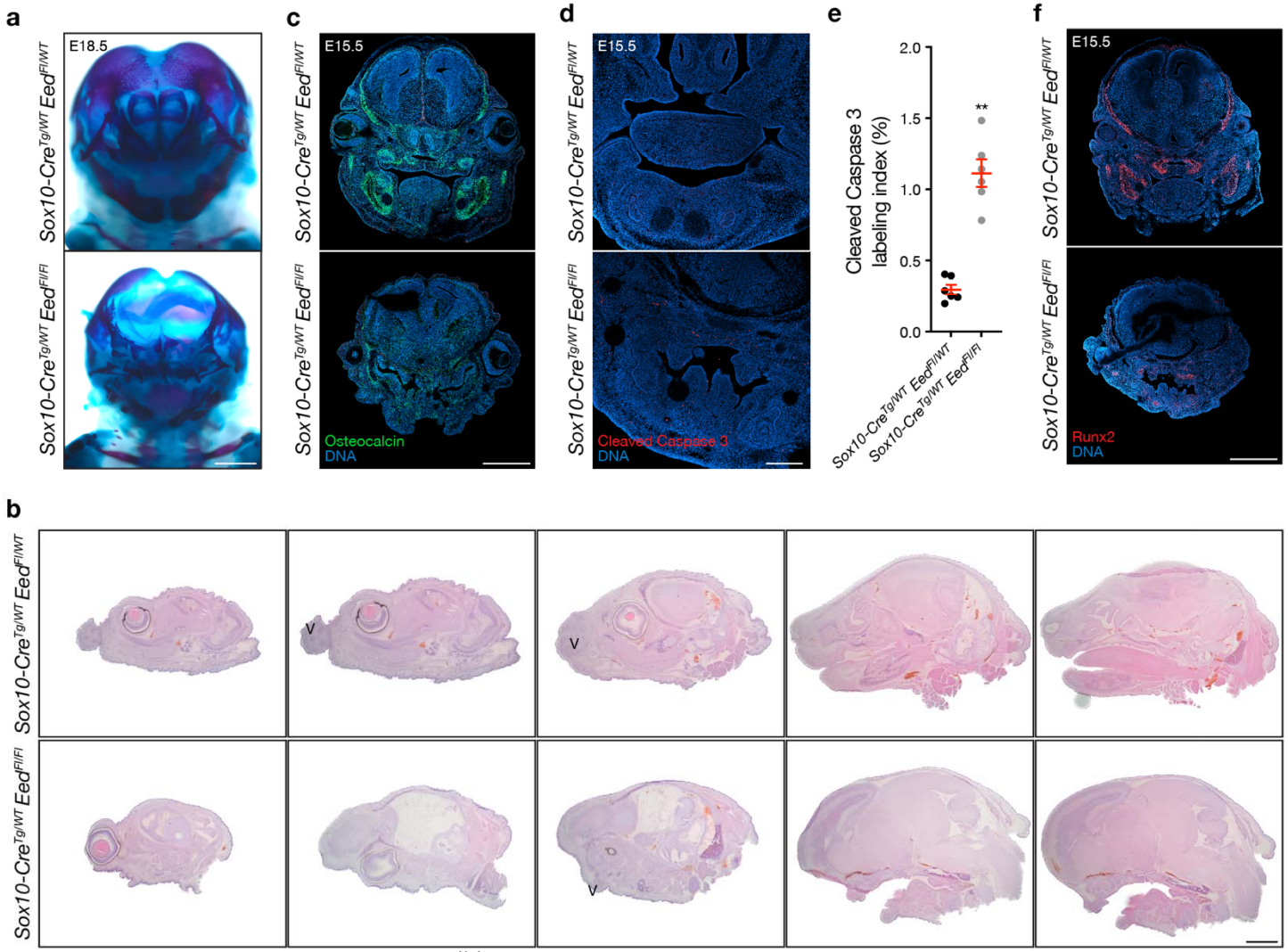

Supplementary Fig. 3. Sox10-Cre Eed$^{Fl/Fl}$ embryos develop significant craniofacial mesenchymal differentiation phenotypes and subtle apoptotic phenotypes. (a) Coronal brightfield images of whole-mount skeletal stains of E18.5 *Sox10-Cre Eed$^{Fl/WT}$* or *Sox10-Cre Eed$^{Fl/Fl}$* embryos. Scale bar, 1mm. (b) Brightfield sagittal H&E images of E16.5 *Sox10-Cre Eed$^{Fl/WT}$* or *Sox10-Cre Eed$^{Fl/Fl}$* heads in series from lateral (left) to medial (right). Vibrissa (V) were reduced in *Sox10-Cre Eed$^{Fl/Fl}$* heads compared to controls. Scale bar, 1mm. (c) Coronal immunofluorescence images of E15.5 *Sox10-Cre Eed$^{Fl/WT}$* or *Sox10-Cre Eed$^{Fl/Fl}$* heads stained for osteocalcin (green). Scale bar, 1mm. (d) Coronal immunofluorescence images of E15.5 *Sox10-Cre Eed$^{Fl/WT}$* or *Sox10-Cre Eed$^{Fl/Fl}$* mandibles stained for Cleaved Caspase 3 (red). Scale bar, 100µm. (e) Quantification of Cleaved Caspase 3 immunofluorescence labeling index from E15.5 *Sox10-Cre Eed$^{Fl/WT}$* or *Sox10-Cre Eed$^{Fl/Fl}$* mandibles. Lines represent means and error bars represent standard error of the means. Student's t-test, **$p \leq 0.01$. (f) Coronal immunofluorescence images of E15.5 *Sox10-Cre Eed$^{Fl/WT}$* or *Sox10-Cre Eed$^{Fl/Fl}$* heads stained for Runx2 (red). Scale bar, 1mm. All images are representative of ≥3 biological replicates. DNA is marked by DAPI.

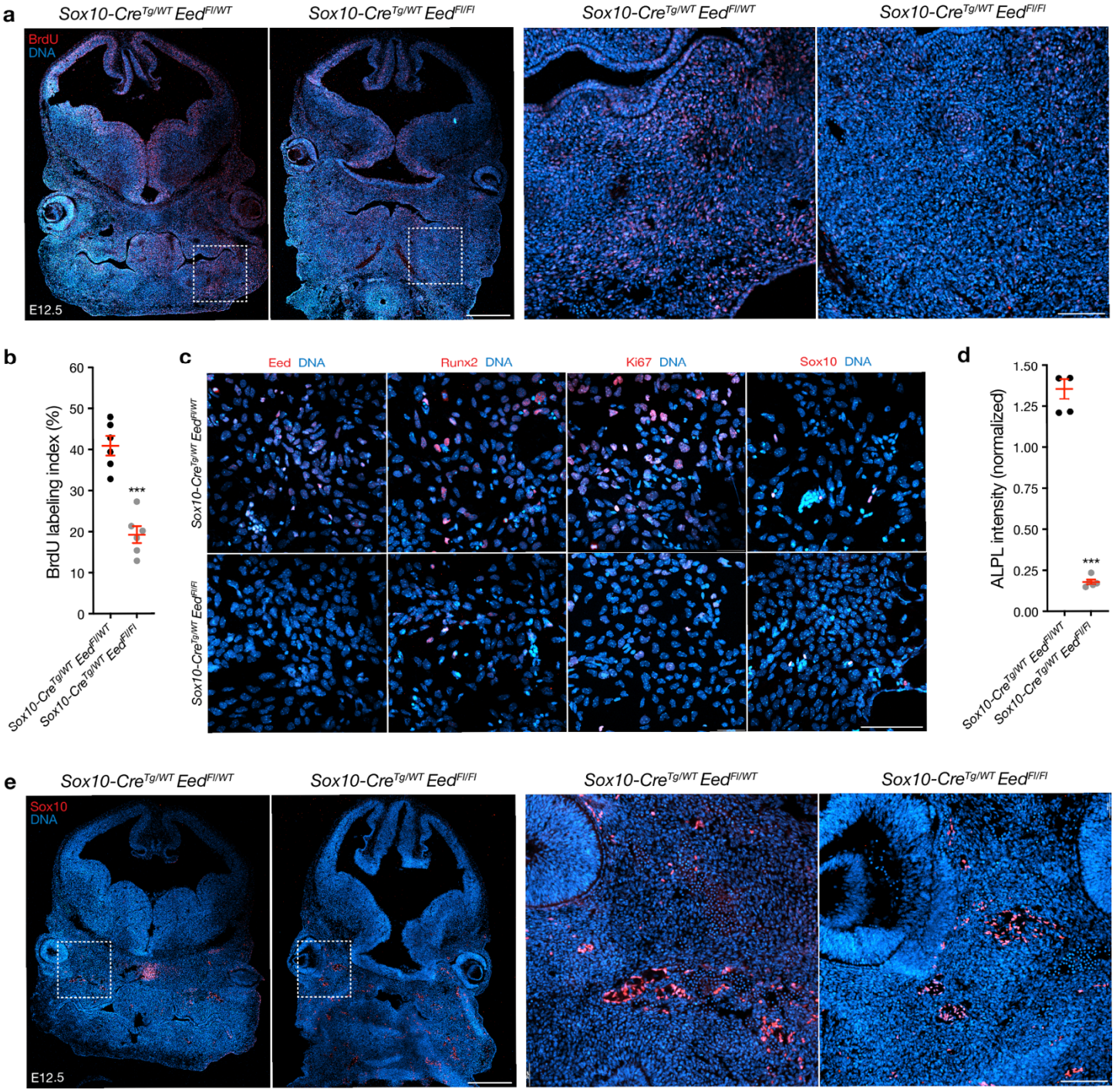

Supplementary Fig. 4. Eed regulates craniofacial differentiation and proliferation in vivo and in primary cell cultures. (a) Coronal immunofluorescence images of E12.5 *Sox10-Cre Eed$^{Fl/WT}$* or *Sox10-Cre Eed$^{Fl/Fl}$* heads stained for BrdU (red). Scale bars, 500µm and 50µm. (b) Quantification of BrdU immunofluorescence labeling index from E12.5 heads. (c) Immunofluorescence images of primary craniofacial cell cultures from E12.5 *Sox10-Cre Eed$^{Fl/WT}$* or *Sox10-Cre Eed$^{Fl/Fl}$* embryos stained for Eed, Runx2, Ki67, or Sox10. Scale bar, 100µm. (d) Quantification of ALPL immunofluorescence imaging intensity from primary E15.5 craniofacial cell cultures. (e) Coronal immunofluorescence images of E12.5 *Sox10-Cre Eed$^{Fl/WT}$* or *Sox10-Cre Eed$^{Fl/Fl}$* heads stained for Sox10 (red). Scale bars, 500µm and 50µm. All images are representative of ≥3 biological replicates. DNA is marked by DAPI. Lines represent means and error bars represent standard error of the means. Student's t-tests, ***$p \leq 0.0001$.

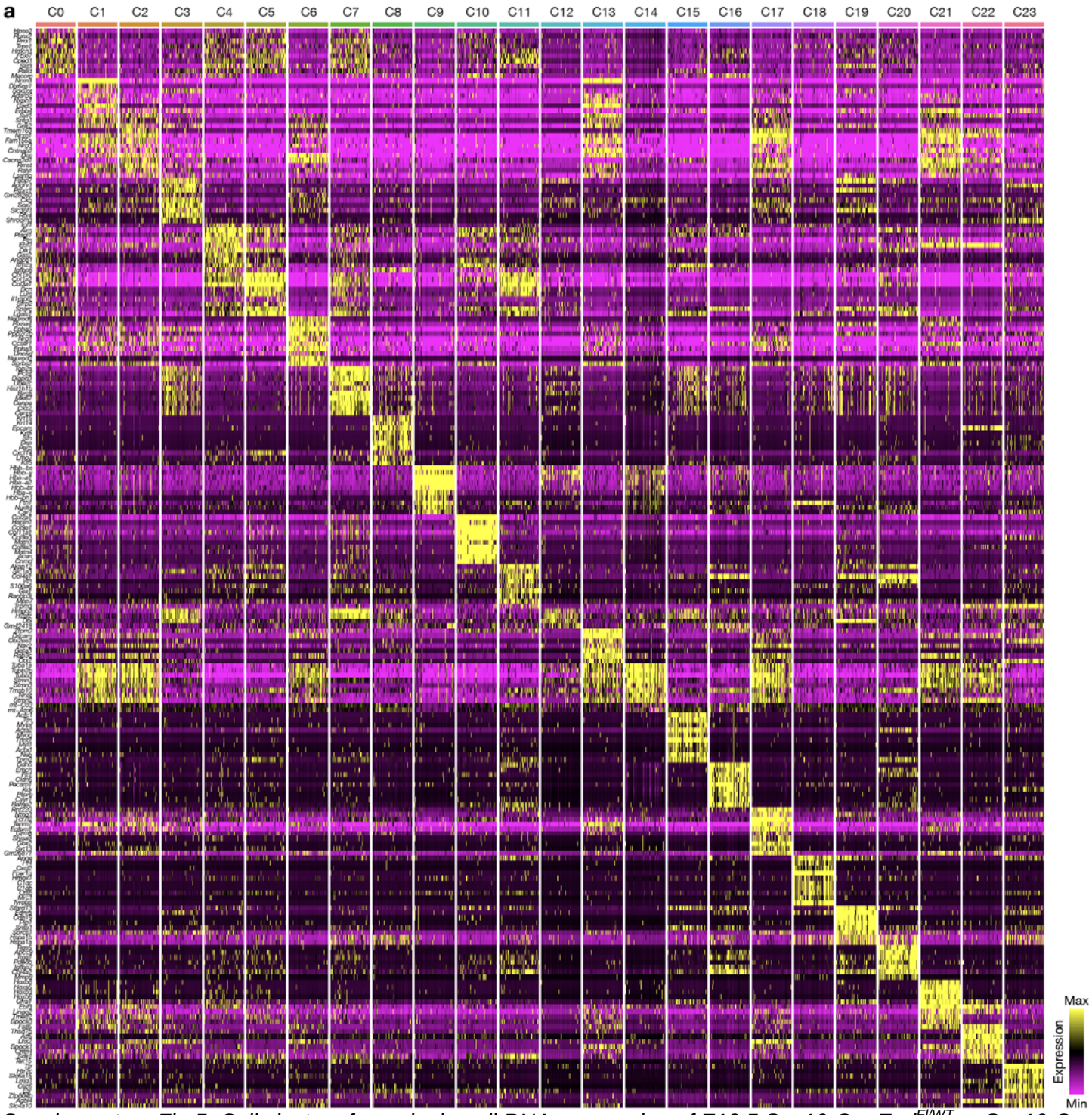

Supplementary Fig 5. Cell clusters from single-cell RNA sequencing of E12.5 Sox10-Cre Eed$^{Fl/WT}$ or Sox10-Cre Eed$^{Fl/Fl}$ heads. (a) Heat map of differentially expressed genes across 23 cell clusters.

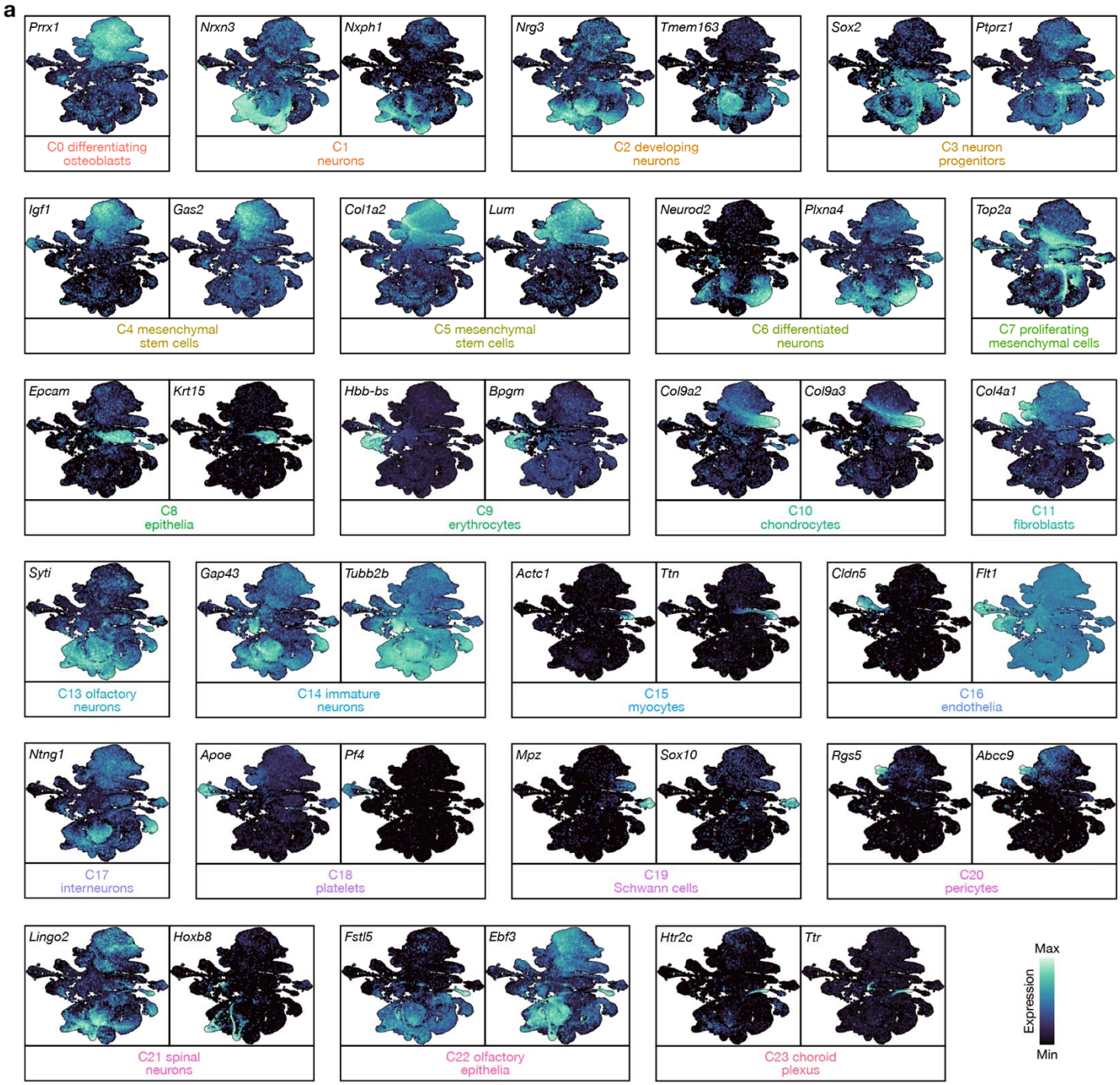

Supplementary Fig. 6. Cell cluster marker genes from single-cell RNA sequencing of E12.5 Sox10-Cre Eed$^{Fl/WT}$ or Sox10-Cre Eed$^{Fl/Fl}$ heads. (a) Gene expression feature plots for differentially expressed genes across 23 cell clusters.

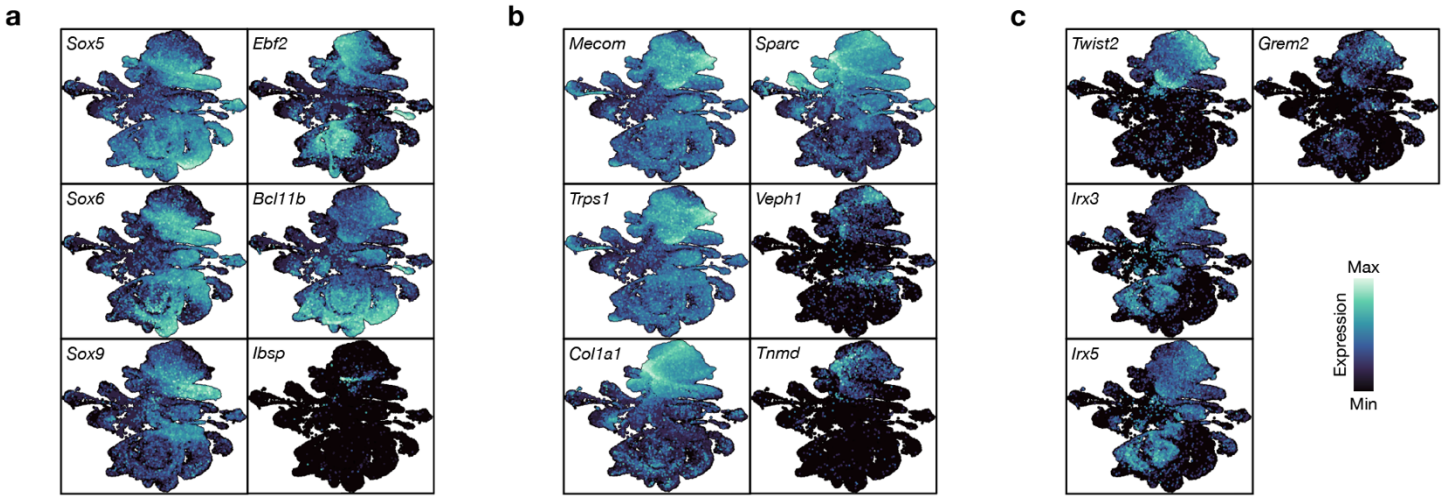

Supplementary Fig. 7. Single-cell transcriptome differential expression analyses among mesenchymal cell clusters. (a) Gene expression feature plots for differentially expressed genes between C0 and C4. (b) Gene expression feature plots for differentially expressed genes between C0 and C5. (c) Gene expression feature plots for differentially expressed genes between mesenchymal stem cell clusters.

Supplementary table titles

Supplementary Table 1. Cell count per embryo and per cell cluster from single-cell RNA sequencing.

Supplementary Table 2. Single-cell RNA sequencing cluster marker genes.

Supplementary Table 3. Differential gene expression between C4 and C0 from single-cell RNA sequencing.

Supplementary Table 4. Differential gene expression between C5 and C0 from single-cell RNA sequencing.

Supplementary Table 5. Differential gene expression between C4 and C5 from single-cell RNA sequencing.

Supplementary Table 6. Differential gene expression between genotypes in C0, C4, C5, and C7 from single-cell RNA sequencing.

Movie captions

Movie 1. B-Mode echocardiography movie of an E16.5 *Sox10-Cre Eed*$^{Fl/WT}$ heart, transversal view at medium level. Both ventricles, external walls, and interventricular septum are visible. Right ventricle is up, and left ventricle is down. The difference in size between ventricles is visible. The ventricular contraction is rhythmic, symmetric, and complete.

Movie 2. B-Mode echocardiography movie of an E16.5 *Sox10-Cre Eed*$^{Fl/Fl}$ heart, transversal view at medium level. Both ventricles, external walls, and interventricular septum are visible. Right ventricle is up, and left ventricle is down. The ventricular contraction is rhythmic and symmetric.

Movie 3. Three-dimensional reconstruction of computed tomography (microCT) imaging of an E19.5 *Sox10-Cre Eed*$^{Fl/WT}$ head.

Movie 4. Three-dimensional reconstruction of computed tomography (microCT) imaging of an E19.5 *Sox10-Cre Eed*$^{Fl/Fl}$ head.

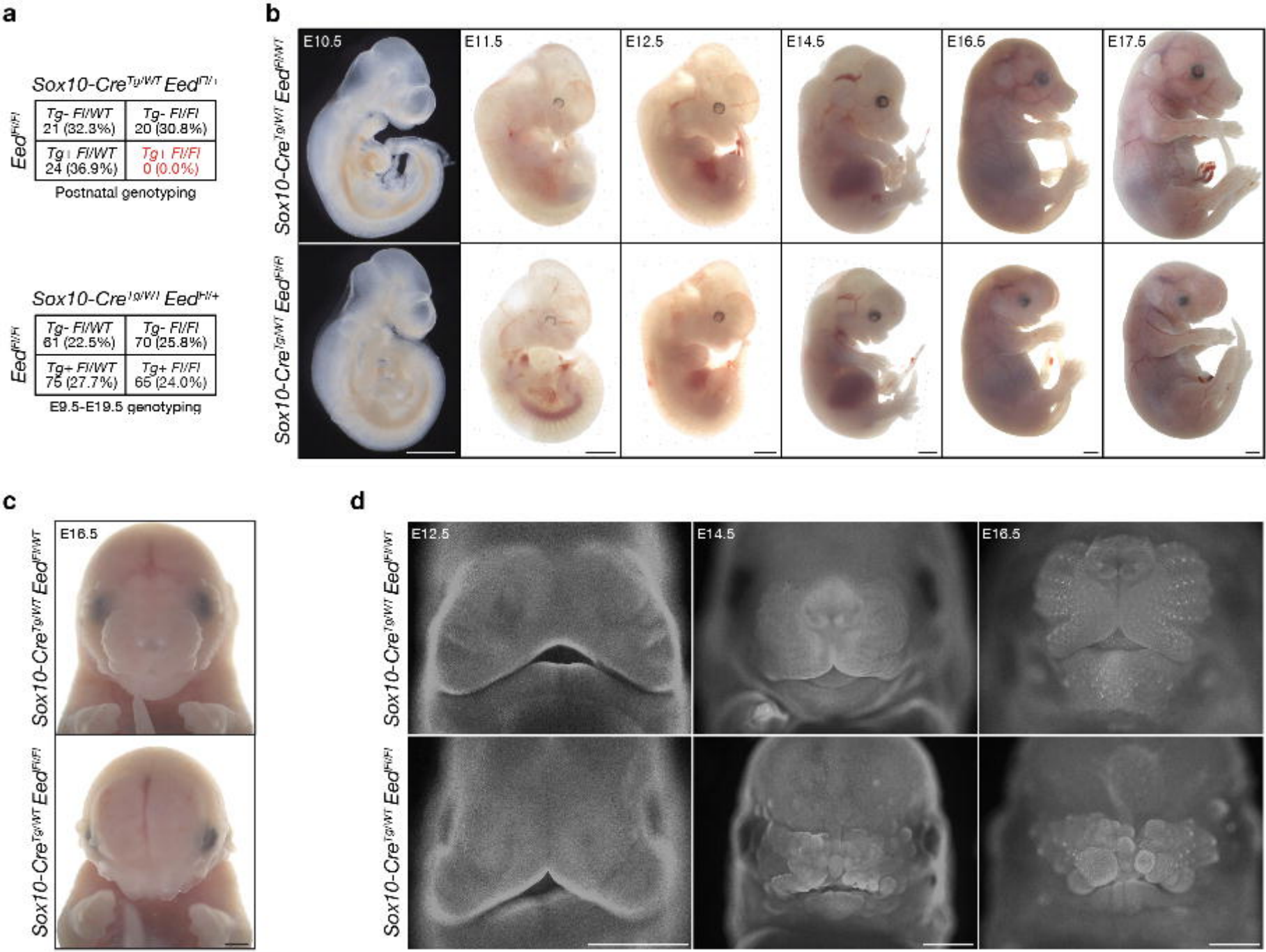
a
Sox10-Cre$^{Tg/WT}$ Eed$^{Fl/+}$
Eed$^{Fl/Fl}$
Tg- Fl/WT 21 (32.3%)
Tg- Fl/Fl 20 (30.8%)
Tg+ Fl/WT 24 (36.9%)
Tg+ Fl/Fl 0 (0.0%)
Postnatal genotyping
Sox10-Cre$^{Tg/WT}$ Eed$^{Fl/+}$
Eed$^{Fl/Fl}$
Tg- Fl/WT 61 (22.5%)
Tg- Fl/Fl 70 (25.8%)
Tg+ Fl/WT 75 (27.7%)
Tg+ Fl/Fl 65 (24.0%)
E9.5-E19.5 genotyping
b
Sox10-Cre$^{Tg/WT}$ Eed$^{Fl/WT}$
Sox10-Cre$^{Tg/WT}$ Eed$^{Fl/Fl}$
E10.5
E11.5
E12.5
E14.5
E16.5
E17.5
c
Sox10-Cre$^{Tg/WT}$ Eed$^{Fl/WT}$
Sox10-Cre$^{Tg/WT}$ Eed$^{Fl/Fl}$
E16.5
d
Sox10-Cre$^{Tg/WT}$ Eed$^{Fl/WT}$
Sox10-Cre$^{Tg/WT}$ Eed$^{Fl/Fl}$
E12.5
E14.5
E16.5

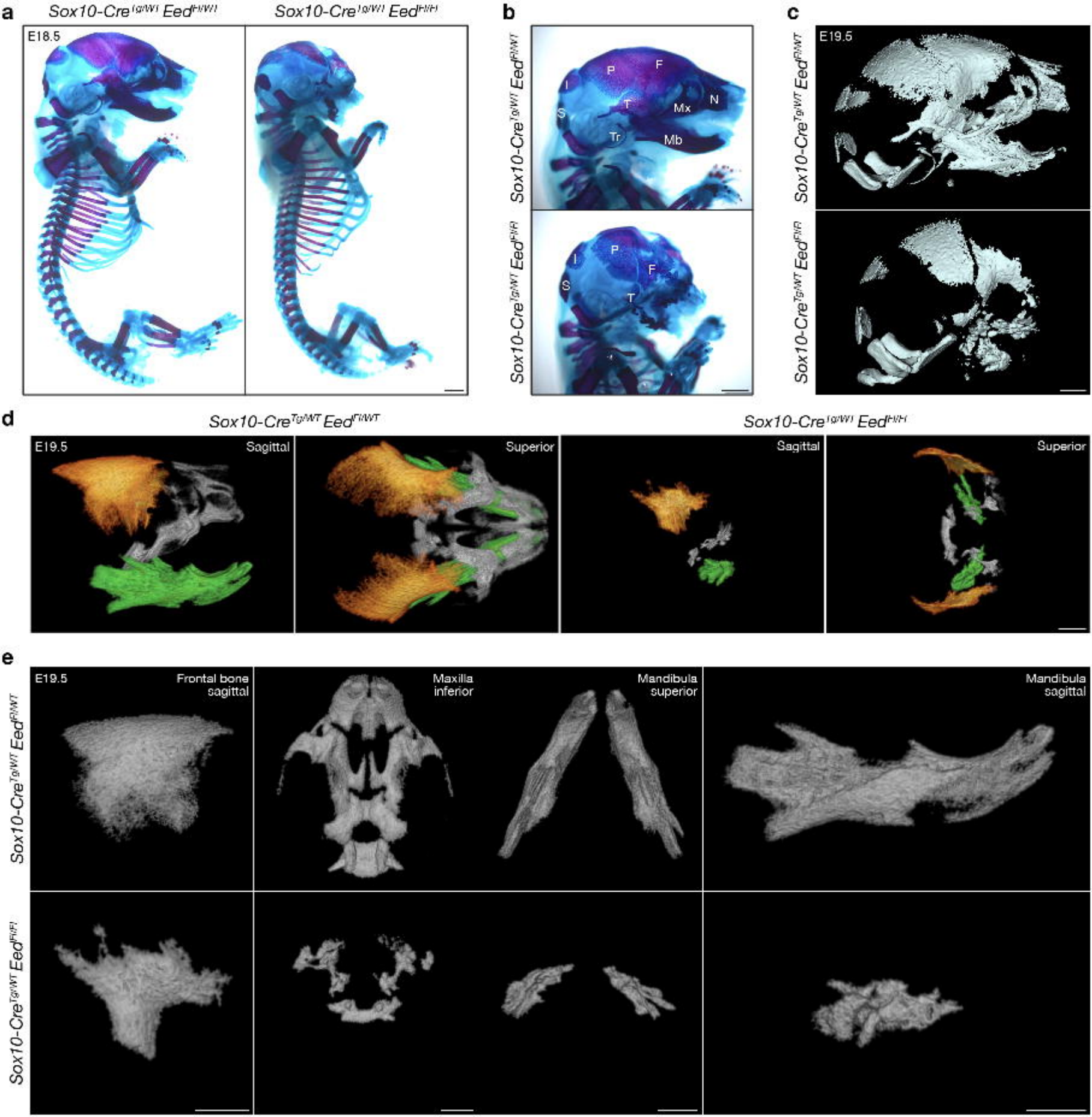
a
Sox10-Cre Tg/WT Eed F/WT
Sox10-Cre Tg/WT Eed F/F
E18.5
b
Sox10-Cre Tg/WT Eed F/WT
Sox10-Cre Tg/WT Eed F/F
P
F
I
T
N
Mx
S
Tr
Mb
c
E19.5
Sox10-Cre Tg/WT Eed F/WT
Sox10-Cre Tg/WT Eed F/F
d
Sox10-Cre Tg/WT Eed F/WT
Sox10-Cre Tg/WT Eed F/F
E19.5
Sagittal
Superior
Sagittal
Superior
e
E19.5
Frontal bone sagittal
Maxilla inferior
Mandibula superior
Mandibula sagittal
Sox10-Cre Tg/WT Eed F/WT
Sox10-Cre Tg/WT Eed F/F

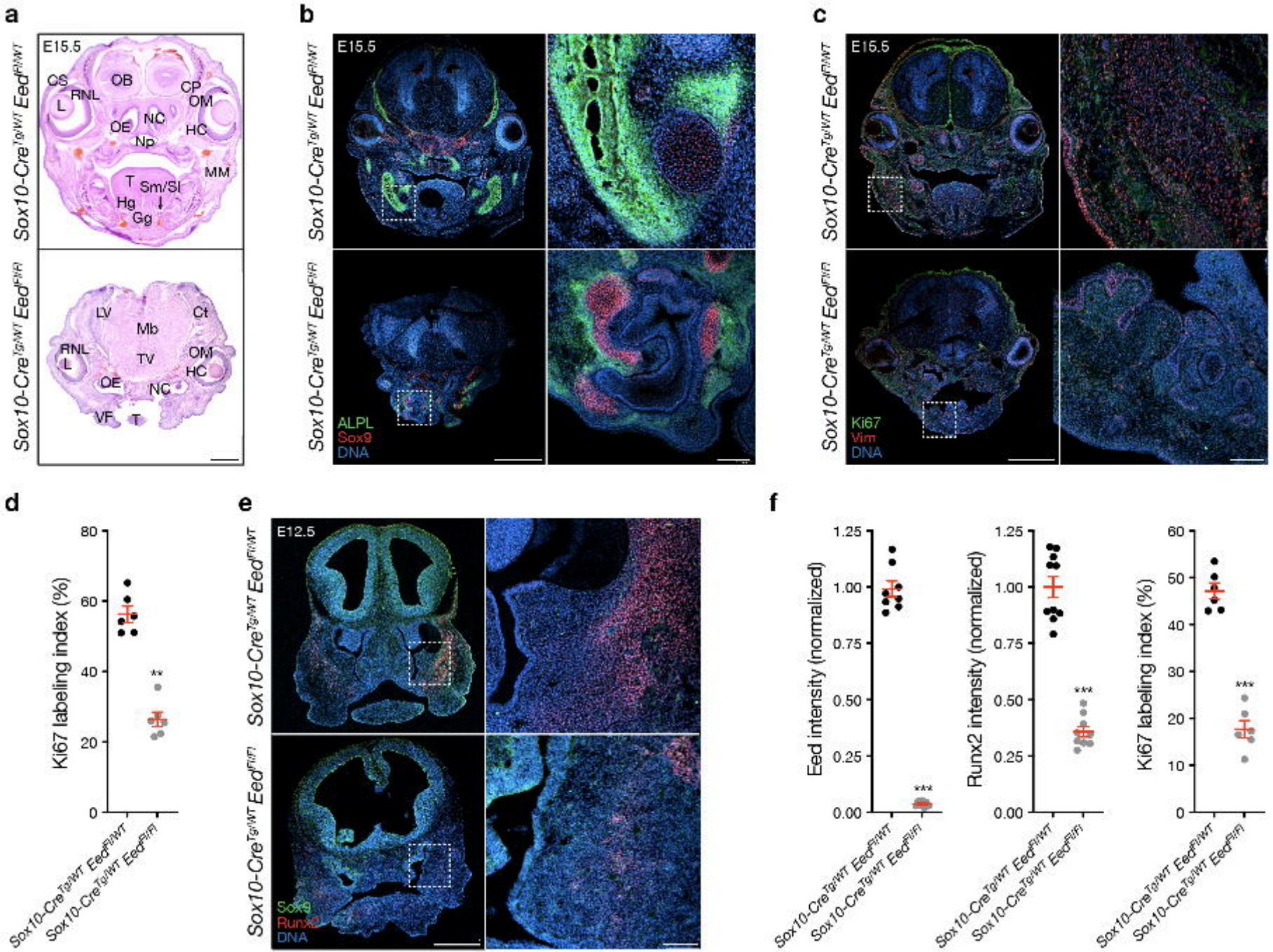
a
E15.5
Sox10-Cre^Tg/WT Eed^Fl/WT
Sox10-Cre^Tg/WT Eed^Fl/Fl
OS
OB
CP
RNL
L
OM
OE
NC
HC
Np
MM
T
Sm/Sl
Hg
Gg
LV
Ct
Mb
RNL
L
TV
OM
HC
OE
NC
VF
T
b
E15.5
ALPL
Sox9
DNA
c
E15.5
Ki67
Vim
DNA
d
Ki67 labeling index (%)
80
60
40
20
0
**
Sox10-Cre^Tg/WT Eed^Fl/WT
Sox10-Cre^Tg/WT Eed^Fl/Fl
e
E12.5
Sox9
Runx2
DNA
f
Eed intensity (normalized)
1.25
1.00
0.75
0.50
0.25
0.00
***
Runx2 intensity (normalized)
Ki67 labeling index (%)
60
50
40
30
20
10
0
Sox10-Cre^Tg/WT Eed^Fl/WT
Sox10-Cre^Tg/WT Eed^Fl/Fl

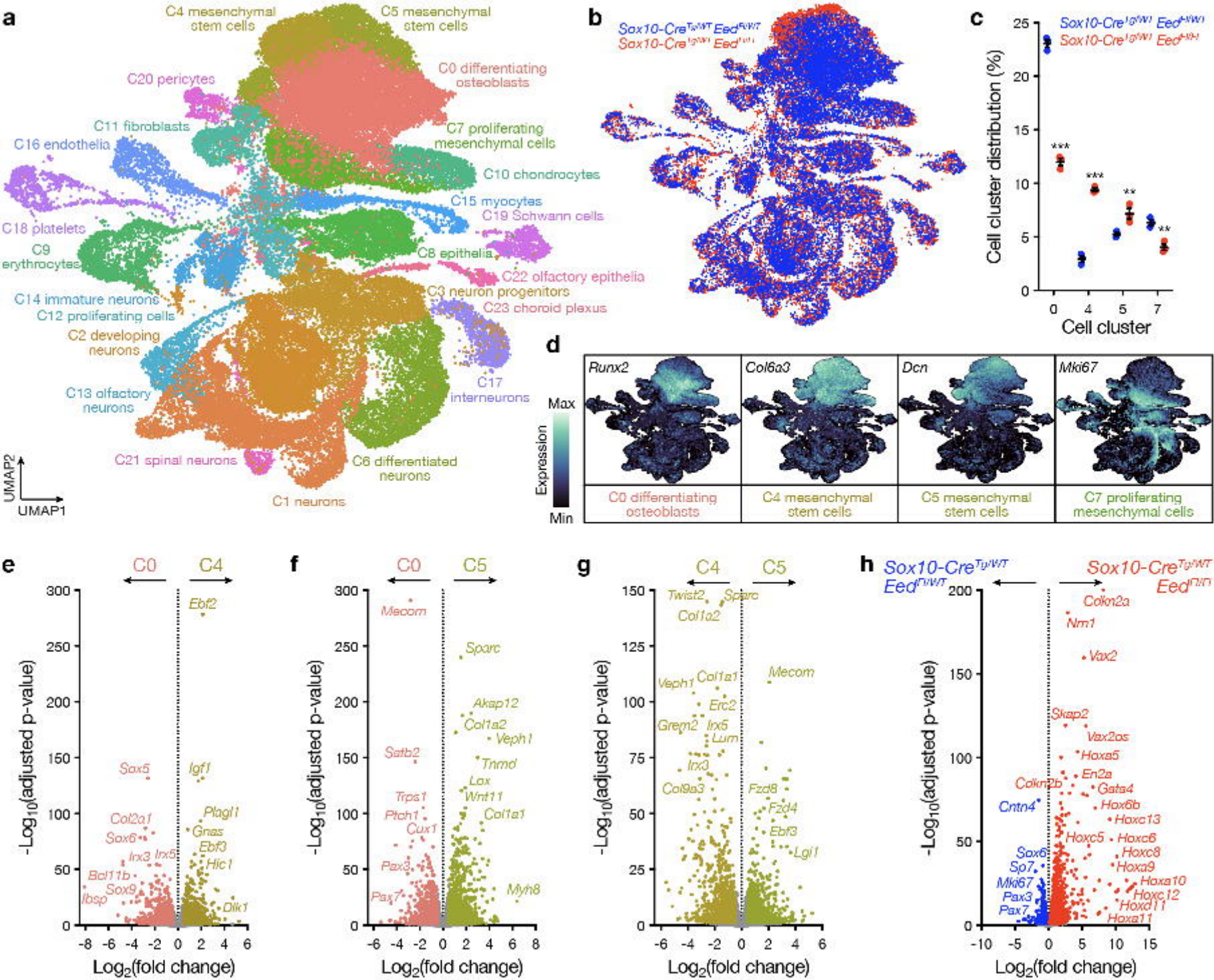
a
C4 mesenchymal stem cells
C5 mesenchymal stem cells
C0 differentiating osteoblasts
C20 pericytes
C11 fibroblasts
C7 proliferating mesenchymal cells
C16 endothelia
C10 chondrocytes
C15 myocytes
C19 Schwann cells
C18 platelets
C9 erythrocytes
C8 epithelia
C22 olfactory epithelia
C3 neuron progenitors
C14 immature neurons
C23 choroid plexus
C12 proliferating cells
C2 developing neurons
C17 interneurons
C13 olfactory neurons
C21 spinal neurons
C6 differentiated neurons
C1 neurons
UMAP2
UMAP1
b
Sox10-Cre^Tg/WT Eed^F/WT
Sox10-Cre^Tg/WT Eed^F/F
c
Sox10-Cre^Tg/WT Eed^F/WT
Sox10-Cre^Tg/WT Eed^F/F
Cell cluster distribution (%)
Cell cluster
d
Runx2
Col6a3
Dcn
Mki67
Max
Expression
Min
C0 differentiating osteoblasts
C4 mesenchymal stem cells
C5 mesenchymal stem cells
C7 proliferating mesenchymal cells
e
C0
C4
-Log10(adjusted p-value)
Log2(fold change)
Ebf2
Sox5
Igf1
Col2a1
Plagl1
Sox6
Gnas
Ebf3
Irx3
Irx5
Hic1
Bcl11b
Sox9
Ibsp
Dlk1
f
C0
C5
Mecom
Sparc
Akap12
Col1a2
Veph1
Satb2
Tnmd
Lox
Trps1
Wnt11
Ptch1
Col1a1
Cux1
Pax3
Pax7
Myh8
g
C4
C5
Twist2
Sparc
Col1a2
Mecom
Veph1
Col1a1
Erc2
Grem2
Irx5
Lum
Irx3
Col9a3
Fzd8
Fzd4
Ebf3
Lgi1
h
Sox10-Cre^Tg/WT Eed^F/WT
Sox10-Cre^Tg/WT Eed^F/F
Cdkn2a
Nrm1
Vax2
Skap2
Vax2os
Hoxa5
En2a
Cdkn2b
Gata4
Cntn4
Hox6b
Hoxc13
Hoxc5
Hoxc6
Hoxc8
Sox6
Hoxa9
Sp7
Hoxa10
Mki67
Hoxc12
Pax3
Hoxd11
Pax7
Hoxa11

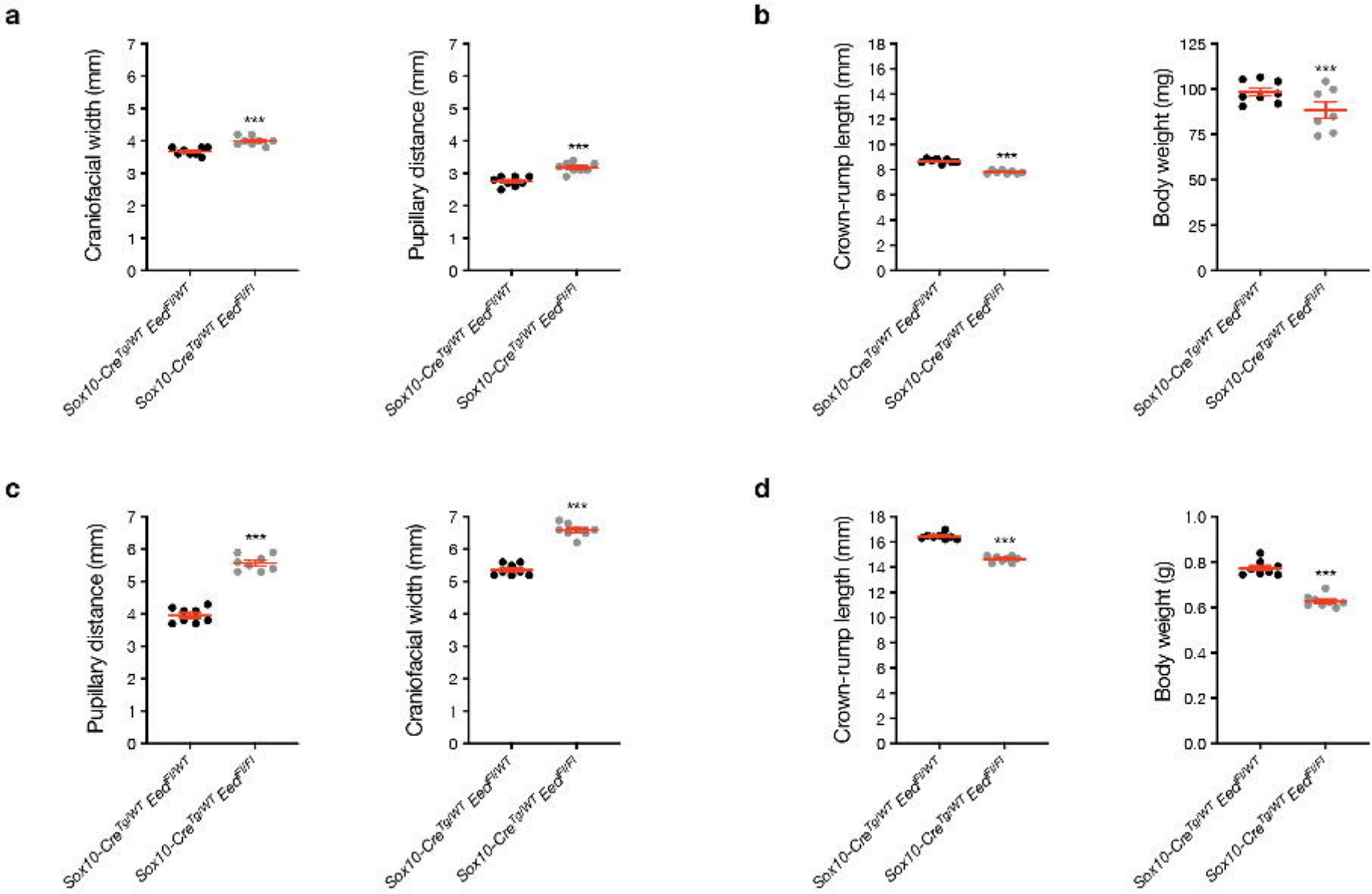
a
Craniofacial width (mm)
Pupillary distance (mm)
b
Crown-rump length (mm)
Body weight (mg)
c
Pupillary distance (mm)
Craniofacial width (mm)
d
Crown-rump length (mm)
Body weight (g)
***
Sox10-Cre^TgWT Eed^FlWT
Sox10-Cre^TgWT Eed^FlFl

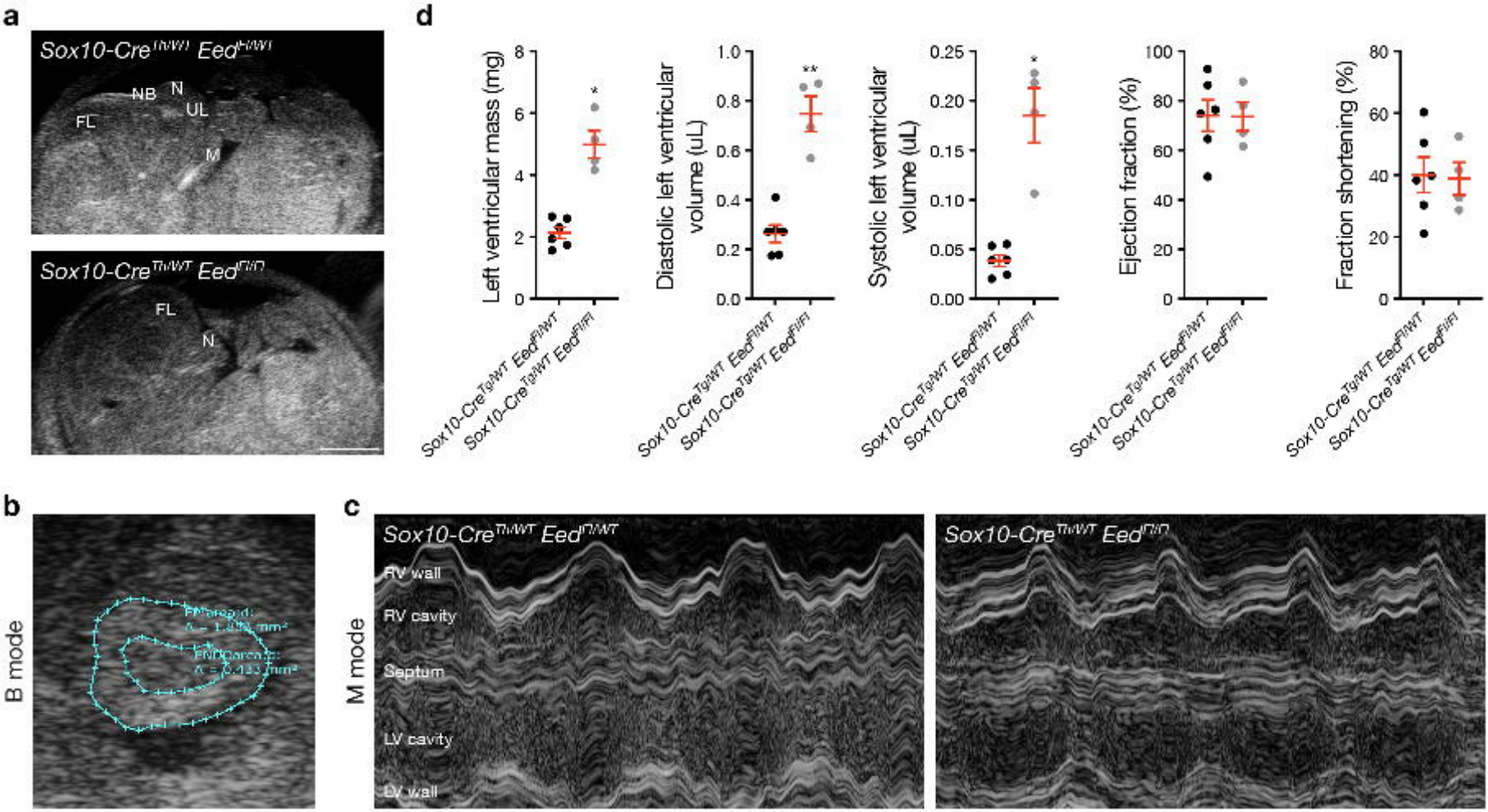
a
Sox10-Cre$^{Tg/WT}$ Eed$^{fl/WT}$
NB
N
UL
FL
M
Sox10-Cre$^{Tg/WT}$ Eed$^{fl/fl}$
FL
N
d
Left ventricular mass (mg)
Diastolic left ventricular volume (uL)
Systolic left ventricular volume (uL)
Ejection fraction (%)
Fraction shortening (%)
Sox10-Cre$^{Tg/WT}$ Eed$^{fl/WT}$
Sox10-Cre$^{Tg/WT}$ Eed$^{fl/fl}$
b
B mode
c
M mode
Sox10-Cre$^{Tg/WT}$ Eed$^{fl/WT}$
RV wall
RV cavity
Septum
LV cavity
LV wall
Sox10-Cre$^{Tg/WT}$ Eed$^{fl/fl}$

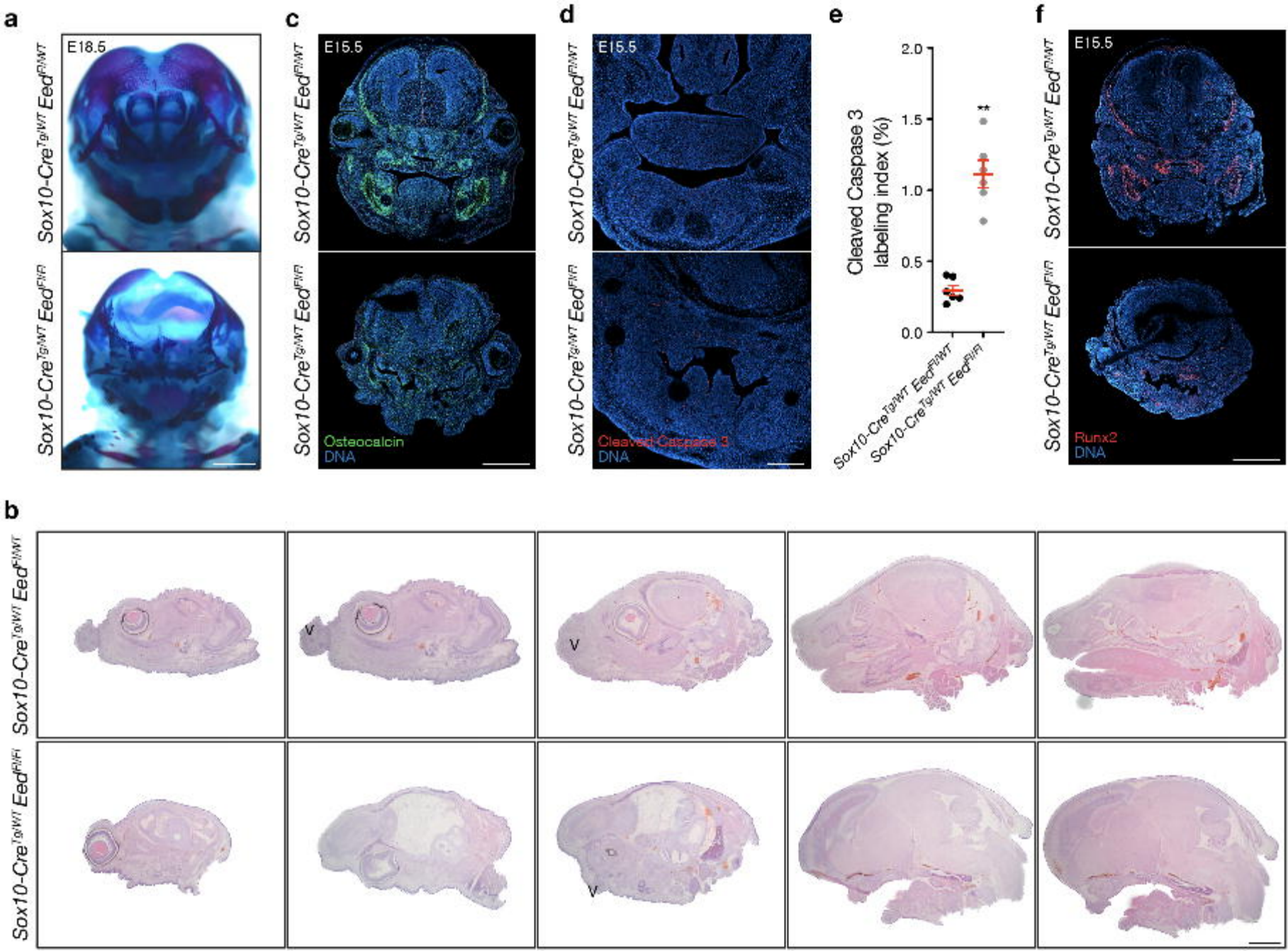
a
E18.5
Sox10-Cre$^{Tg/WT}$ Eed$^{Fl/WT}$
Sox10-Cre$^{Tg/WT}$ Eed$^{Fl/Fl}$
c
E15.5
Osteocalcin
DNA
d
E15.5
Cleaved Caspase 3
DNA
e
Cleaved Caspase 3 labeling index (%)
2.0
1.5
1.0
0.5
0.0
f
E15.5
Runx2
DNA
b
V

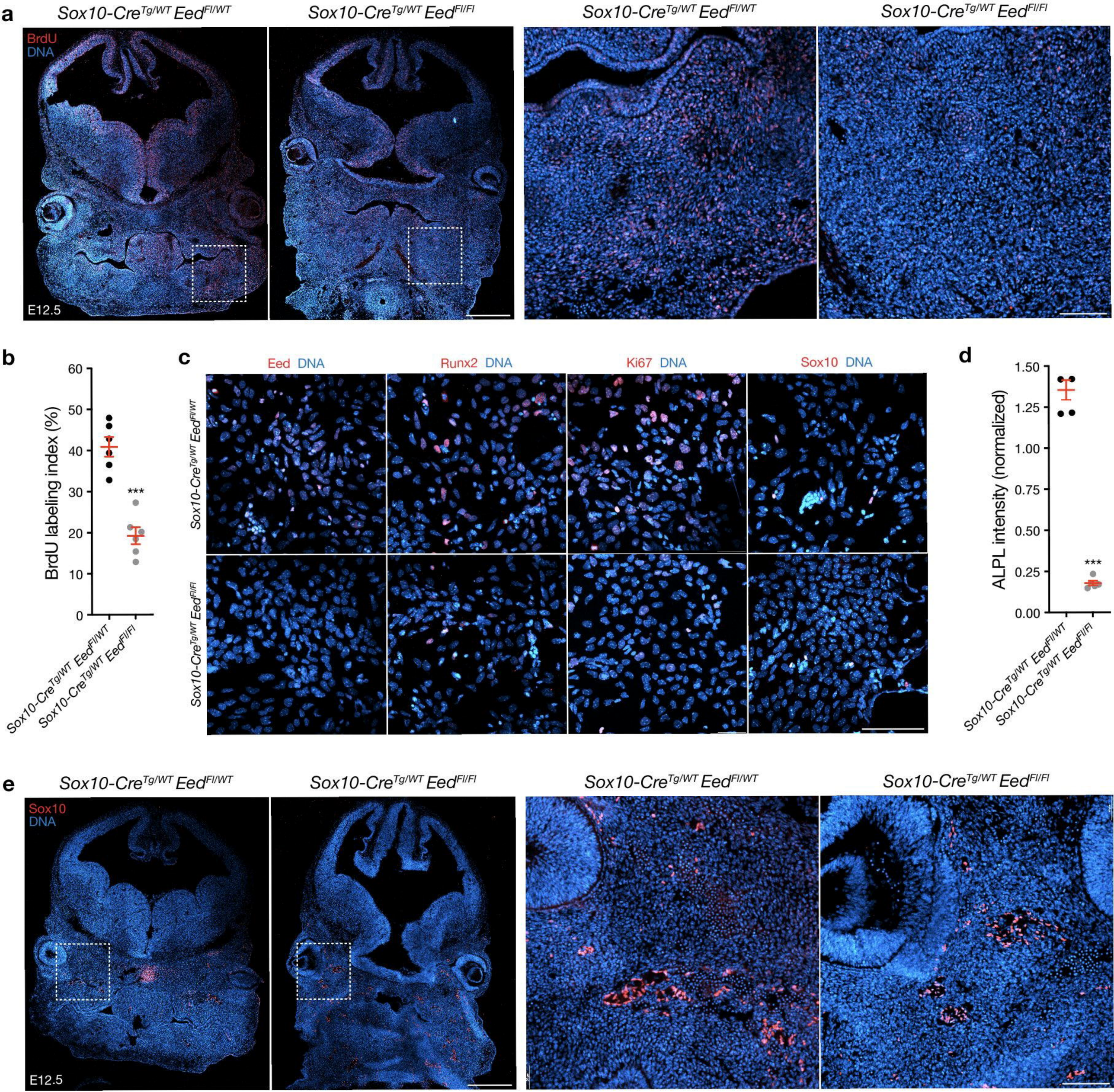
a
Sox10-Cre$^{Tg/WT}$ Eed$^{Fl/WT}$
Sox10-Cre$^{Tg/WT}$ Eed$^{Fl/Fl}$
BrdU
DNA
E12.5
b
BrdU labeling index (%)
60
50
40
30
20
10
0
***
Sox10-Cre$^{Tg/WT}$ Eed$^{Fl/WT}$
Sox10-Cre$^{Tg/WT}$ Eed$^{Fl/Fl}$
c
Eed DNA
Runx2 DNA
Ki67 DNA
Sox10 DNA
Sox10-Cre$^{Tg/WT}$ Eed$^{Fl/WT}$
Sox10-Cre$^{Tg/WT}$ Eed$^{Fl/Fl}$
d
ALPL intensity (normalized)
1.50
1.25
1.00
0.75
0.50
0.25
0.00
***
Sox10-Cre$^{Tg/WT}$ Eed$^{Fl/WT}$
Sox10-Cre$^{Tg/WT}$ Eed$^{Fl/Fl}$
e
Sox10-Cre$^{Tg/WT}$ Eed$^{Fl/WT}$
Sox10-Cre$^{Tg/WT}$ Eed$^{Fl/Fl}$
Sox10
DNA
E12.5

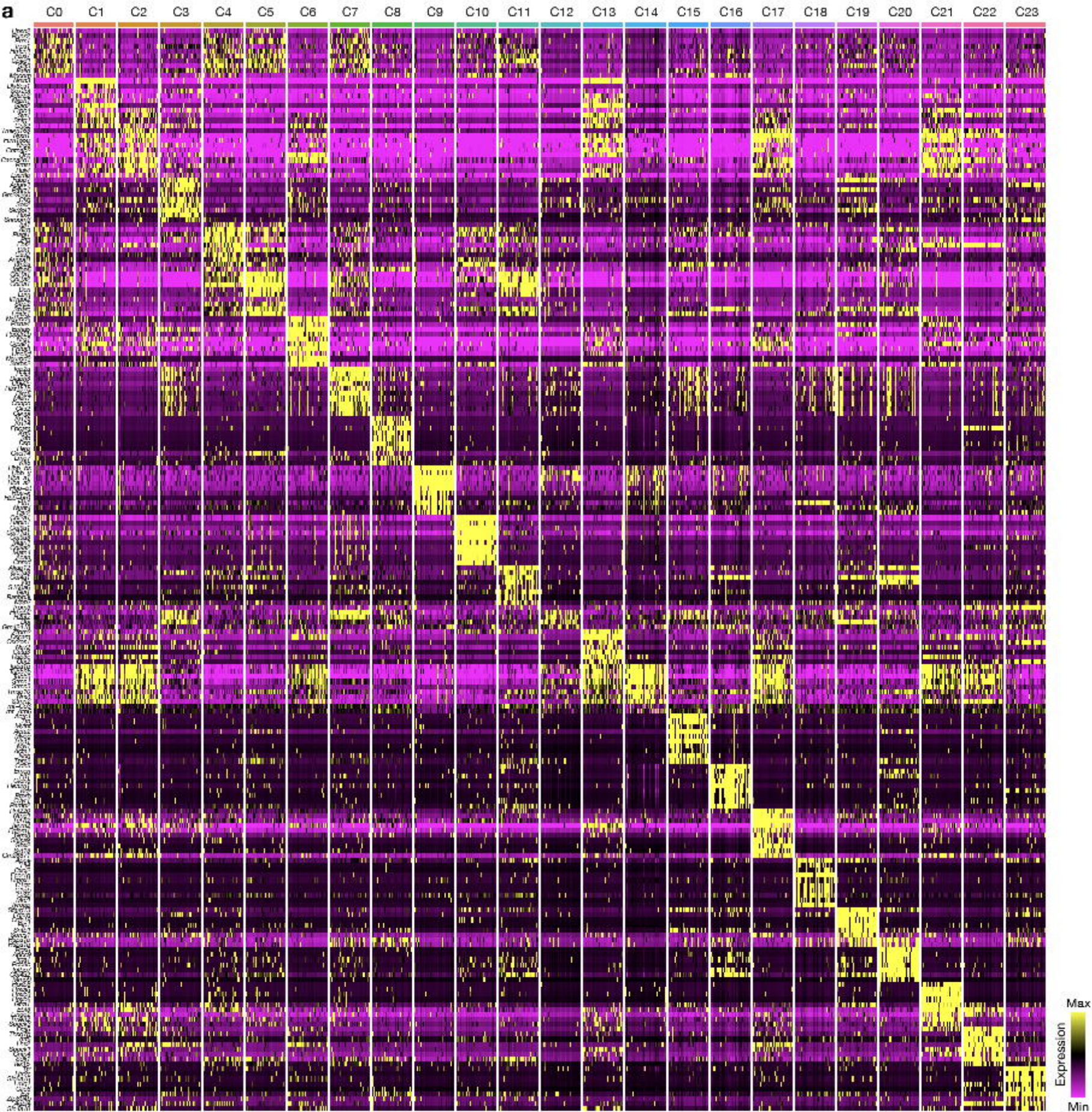
a
C0
C1
C2
C3
C4
C5
C6
C7
C8
C9
C10
C11
C12
C13
C14
C15
C16
C17
C18
C19
C20
C21
C22
C23
Max
Expression
Min

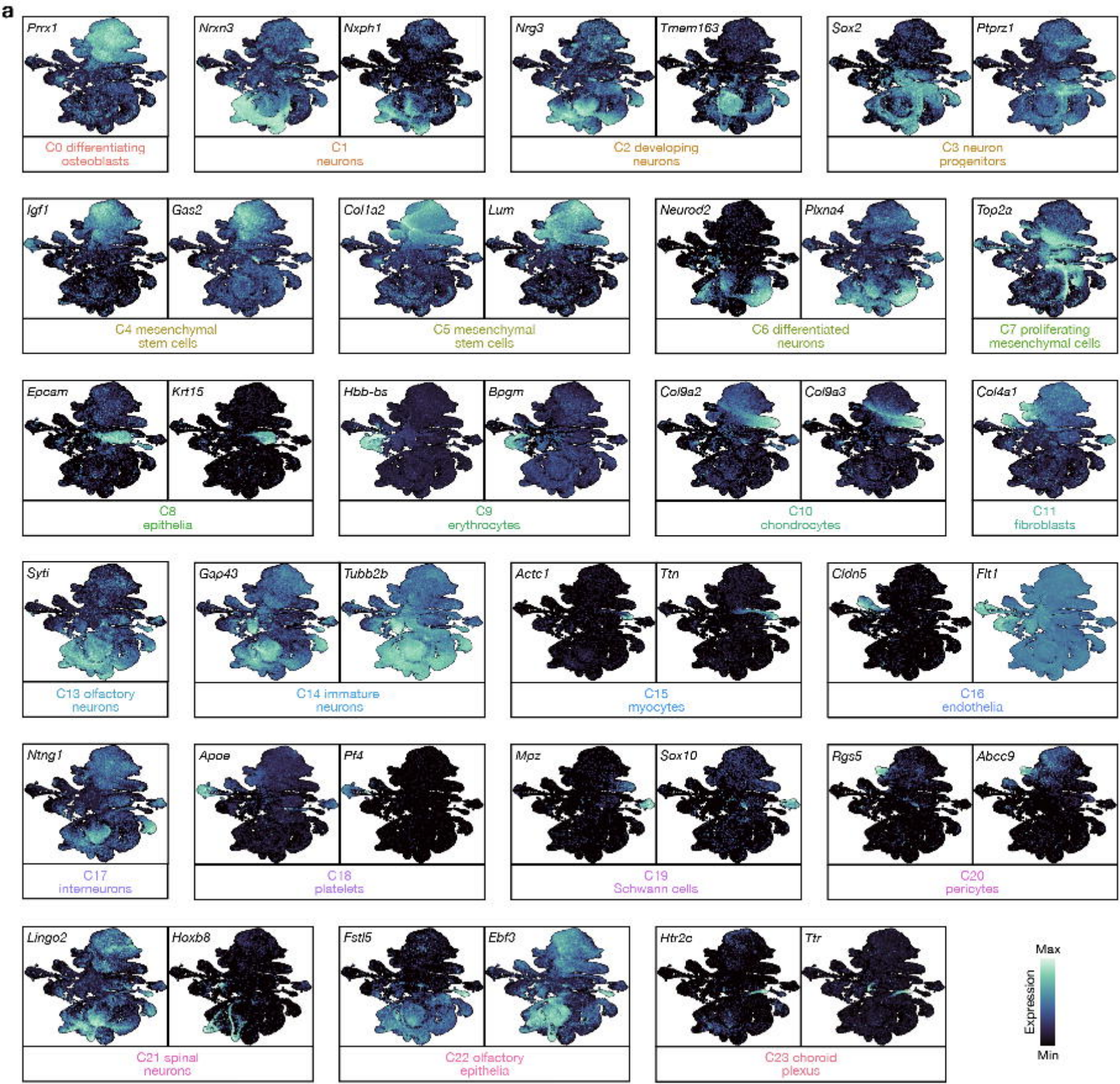
a
Prrx1
C0 differentiating osteoblasts
Nrxn3
Nxph1
C1 neurons
Nrg3
Tmem163
C2 developing neurons
Sox2
Ptprz1
C3 neuron progenitors
Igf1
Gas2
C4 mesenchymal stem cells
Col1a2
Lum
C5 mesenchymal stem cells
Neurod2
Plxna4
C6 differentiated neurons
Top2a
C7 proliferating mesenchymal cells
Epcam
Krt15
C8 epithelia
Hbb-bs
Bpgm
C9 erythrocytes
Col9a2
Col9a3
C10 chondrocytes
Col4a1
C11 fibroblasts
Syti
C13 olfactory neurons
Gap43
Tubb2b
C14 immature neurons
Actc1
Ttn
C15 myocytes
Cldn5
Flt1
C16 endothelia
Ntng1
C17 interneurons
Apoe
Pf4
C18 platelets
Mpz
Sox10
C19 Schwann cells
Rgs5
Abcc9
C20 pericytes
Lingo2
Hoxb8
C21 spinal neurons
Fstl5
Ebf3
C22 olfactory epithelia
Htr2c
Ttr
C23 choroid plexus
Max
Expression
Min

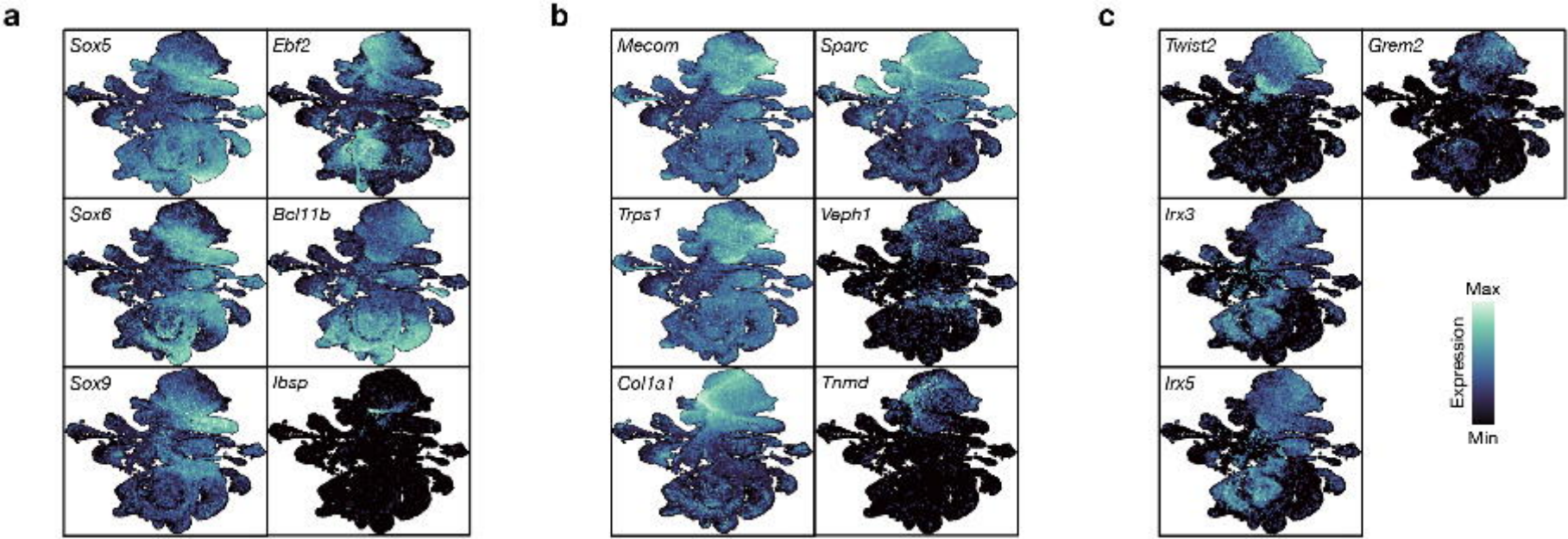
a
Sox5
Ebf2
Sox6
Bcl11b
Sox9
Ibsp
b
Mecom
Sparc
Trps1
Veph1
Col1a1
Tnmd
c
Twist2
Grem2
Irx3
Irx5
Max
Expression
Min